RSC Advances

PAPER

View Article Online
View Journal | View Issue



Cite this: *RSC Adv.*, 2026, **16**, 19903

# Development of a multi-targeted sulfonyl-bridged bisselenadiazole derivative as a potent EGFR/PI3K/AKT/mTOR modulator in lung adenocarcinoma

Wesam Abd El-Fattah,[a] Ahlem Guesmi,*[a] Naoufel Ben Hamadi,[a] Abdelwahed R. Sayed,[b] Ahmed A. M. El-Reedy,[c] Hani S. Hafez,[d] Reda F. M. Elshaarawy *[e] and Soha A. Hassan[d]

Lung adenocarcinoma (LUAD), the most common type of non-small cell lung cancer (NSCLC), requires multi-targeted therapies to overcome resistance mechanisms and reduce toxicity. Herein, we synthesize and characterize a new sulfonyl-bridged bis(1,3,4-selenadiazole) derivative (BISDA) containing four pharmacophores that potently inhibits LUAD cell proliferation. BISDA displayed 48-h $IC_{50}$ of 2.609 μg $mL^{-1}$ in A549 cells, decreased viability compared to controls, and was less toxic than cisplatin while inducing apoptosis, G2/M cell cycle arrest, and inhibiting cancer cell migration. BISDA remodels the redox environment by reducing glutathione peroxidase activity, and increasing intracellular glutathione levels, leading to increased PD-1 and reduced IFN-γ expression. It further downregulated prominent oncogenic drivers, EGFR, AKT1, MAPK3, mTOR, TGF β, HSP60, HSP70 and HSP90, targeting proliferation and survival with stress response in the context of metastasis. Principal component analysis showed that BISDA reprogrammed signaling through decoupling of the EGFR–mTOR axis from the TGFβ–AKT1–MAPK3–HSP90 cluster, indicative of a global rewiring of pathways. These results suggest that BISDA may serve as a multifaceted inhibitor for treating LUAD, acting in an antiproliferative capacity through apoptosis induction while also preventing signaling pathways associated with resistance.

Received 9th March 2026
Accepted 30th March 2026

DOI: 10.1039/d6ra02006b

rsc.li/rsc-advances



## 1 Introduction

According to GLOBOCAN, lung cancer results in 2480675 new cases and 1817469 deaths worldwide.[1] Non-small cell lung cancer (NSCLC), specifically lung adenocarcinoma (LUAD), is the most prevalent type, affecting both smokers and non-smokers through genetic mutations and chemical exposure.[2] Current chemotherapies exhibit significant toxicity and resistance, necessitating novel agents with enhanced efficacy and reduced off-target effects.[3] To address these limitations, we present a multifunctional derivative designed to target multiple oncogenic pathways.

Synthetic compounds represent potential therapeutic agents targeting cancer signal transduction pathways. The epidermal growth factor receptor (EGFR) is a receptor tyrosine kinase that regulates cell growth, survival, and differentiation. Upon epidermal growth factor (EGF) binding, EGFR undergoes dimerization and autophosphorylation, activating the PI3K/AKT/mTOR and RAS/RAF/MAPK/ERK pathways.[4] The PI3K/AKT/mTOR pathway controls cellular proliferation, growth, migration, and apoptosis resistance,[5] while the RAS/RAF/MAPK/ERK pathway regulates cell proliferation, apoptosis, differentiation, and stress response. Disruption of these components can lead to tumor development.[5] Studies have demonstrated that synthetic azole derivatives exhibit greater efficacy than doxorubicin in colorectal and lung adenocarcinoma cells *via* the EGFR and PI3K/AKT/mTOR pathways and are considered safer than traditional chemotherapies.[6]

Heterocyclic compounds containing selenium are rare but attract interest due to their reactivity and potential in cancer therapy. Selenadiazoles exhibit anticancer properties and stimulate mitochondrial apoptosis *via* JAK2/STAT3 cascades in breast MCF7 and HeLa cancer cells.[7,8] Sulfone derivatives display anticancer activity in LUAD,[9] leukemia,[10] and head and neck squamous cell carcinoma[11] by modulating proliferation pathways. Chalcones exhibit anticancer activity *via* ferroptosis in LUAD cells[12] and inhibit migration through G2/M cell cycle arrest in bone, hepatic, and lung cancer cells.[13] Imino compounds act as antitumor agents by suppressing tubulin

[a]*Chemistry Department, College of Science, Imam Mohammad Ibn Saud Islamic University (IMSIU), P. O. Box 5701, Riyadh 11432, Saudi Arabia. E-mail: amalkasme@imamu.edu.sa*

[b]*Institute of Basic and Applied Science, Egypt-Japan University of Science and Technology, Alexandria, Egypt. E-mail: abdelwahed.rashad@ejust.edu.eg*

[c]*Basic-Applied Science Department, Faculty of Oral and Dental Medicine, Nahda University, Beni-Suef, Egypt*

[d]*Deparment of Zoology, Faculty of Science, Suez University, 43518 Suez, Egypt. E-mail: hani.hafez@suezuniv.edu.eg; Soha.Hassan@suezuniv.edu.eg*

[e]*Department of Chemistry, Faculty of Science, Suez University, 43533 Suez, Egypt. E-mail: reda.elshaarawy@suezuniv.edu.eg*

polymerization[14,15] and inhibiting carbohydrate enzymes in cancer cells.[16]

Programmed cell death protein 1 (PD-1) is a transmembrane receptor expressed on immune cells that regulates immune responses.[17] PD-1 binding to PD-L1 and PD-L2 inhibits T lymphocyte activation and promotes immune tolerance, thereby enabling cancer cells to evade immunity in non-small cell lung cancer (NSCLC). PD-L1 expression is regulated by the EGFR/MAPK pathway.[18] PD1 and PDL1 are important targets for NSCLC immunotherapy, with immune checkpoint inhibitors (ICIs) blocking PD1 or PDL1 to enhance antitumor immunity.[19] Consequently, PD-1 and PD-L1 may serve as biomarkers of therapeutic effectiveness. Interferon gamma (IFN-γ) acts as a cancer biomarker, predicting therapeutic efficacy through tumor recognition with ICIs,[20,21] while its activation promotes tumor progression *via* anti-apoptotic and metastatic effects by stimulating the EGFR and MAPK/ERK pathways in brain cancer and intestinal cells.[22]

Although advancements have been made, existing therapies for LUAD frequently encounter obstacles, including the development of resistance to targeted treatments and significant systemic toxicity from traditional chemotherapy drugs. Consequently, there is a critical need for innovative, multi-functional compounds capable of overcoming these challenges by effectively targeting multiple cancer-related pathways while offering enhanced safety profiles. Therefore, the development of novel synthetic chemical compounds containing selenadiazole, sulfone, ketone, aromatic ring, and imino derivatives (BISDA) represents a strategic approach to address critical gaps in current anticancer therapy through multi-targeted molecular design, incorporating antioxidant, cell cycle arrest, apoptosis triggering, IFN-γ, and EGFR inhibition with PD-1 activation. The synthesized compound was designed to circumvent drug resistance associated with conventional chemotherapeutics through apoptosis evasion and to mitigate poor tumor selectivity, which can lead to severe systemic toxicity. Our study aimed to develop novel multi-target agents by synthesizing a bis selenadiazolimine derivative (BISDA), integrating these functional groups to enhance efficacy and reduce resistance to LUAD treatment, utilizing the A549 cell line as an *in vitro* model.

BISDA comprises four pharmacophores (sulfone, 1,3,4-selenadiazole, imino and arylketone moieties), which were integrated to generate complementary anticancer actions. The sulfone-bridged aromatic scaffold is a rigid, electron withdrawing and lipophilic backbone that assists in stabilizing the conjugated system while also promoting protein target intermolecular interactions that allow for redox-active behavior across the π-framework.[23,24] On the other hand, selenium from 1,3,4-selenadiazole rings that can induce intracellular redox imbalance and trigger ROS release in cancer cells sensitizes the redox-prone signaling hubs such as EGFR/PI3K/AKT/mTOR and stress-response pathways.[8] The imino functions perform hydrogen-bond donor/acceptor and coordination sites that interact with nucleophilic residues in enzymes and molecular chaperones, including heat shock proteins, resulting in modulated apoptosis and cell cycle control.[25,26] The arylketone moieties extend conjugation and increase planarity, facilitating π–π stacking with aromatic amino acid residues and nucleic acids, while tuning the electronic distribution throughout the scaffold.[26,27] This constellation of functional groups links selenium-induced redox perturbation to inhibition of pro-survival and stress-adaptation pathways but endows attributes that enable DNA/protein binding. This multitarget strategy is designed to elicit oxidative stress, inhibit related pathways of EGFR/AKT/mTOR and heat shock protein (HSP) signaling, and stimulate apoptosis, G2/M cell cycle arrest process as well as migration inhibition effects in lung adenocarcinoma cells.

# 2 Materials and methods

## 2.1. Chemistry

**2.1.1. Chemicals and reagents.** All chemicals, reagents, and solvents used in this study were obtained from commercial sources and utilized directly without further purification. 3-Chloro-2,4-pentanedione (97%), 4,4′-diaminodiphenyl sulfone (98%), and potassium selenocyanate (97%) were obtained from Sigma-Aldrich. Sodium acetate trihydrate (99%) and sodium nitrite (98%) were obtained from Thermo Fisher Scientific.

**2.1.2. Instrumentations.** The melting points of the new compounds were determined using an Electrothermal IA 9000 series digital melting point apparatus. Fourier transform infrared (FTIR) spectra were recorded as KBr discs in the range of 400–4000 $cm^{-1}$ using a Pye Unicam SP 3300 and a Shimadzu FTIR 8101 PC spectrophotometer. Absorption bands were denoted as weak (w), medium (m), strong (s), broad (br), and sharp (sh). A Varian Mercury VX-300 spectrometer was used to acquire the NMR spectra. The instrument was run at 300 MHz for $^{1}$H-NMR and at 75 MHz for $^{13}$C-NMR. Deuterated dimethyl sulfoxide (DMSO-$d_6$) was used as solvent. The $^{1}$H NMR signal at 2.52 ppm and the $^{13}$C NMR signal at 39.5 ppm of residual DMSO-$d_6$ proton were used to calibrate the spectrometer. Splitting patterns of the NMR peaks were represented as singlet (s), doublet (d), triplet (t), quartet (q), or multiplet (m).

**2.1.3. Synthesis *N*,*N*′-((sulfonyl)-bis(1,4-phenylene))bis(2-oxopropanehydrazonoyl chloride) (BHC).** The intermediate bishydrazonoyl chloride (BHC) was synthesized following the established procedure reported in our previous work.[28] In brief, 4,4′-diaminodiphenyl sulfone (DADPS, 2.48 g, 10 mmol) in 6 M hydrochloric acid (6 mL), was dissolved and cooled to 0–5 °C using an ice bath while stirring with a magnetic stirring bar. The diazonium salt was generated *in situ* by adding freshly prepared aqueous sodium nitrite (0.69 g, 10 mmol in 10 mL distilled water, 0.71% w/v) dropwise over a period of 5 min. To ensure complete diazotization, the reaction mixture was stirred vigorously for 20 min at 0–5 °C. A 250 mL round bottom flask was charged with 3-chloro-2,4-pentanedione (1.34 g, 10 mmol) and anhydrous sodium acetate trihydrate (1.36 g, 10 mmol), then dissolved in absolute ethanol (100 mL) under a simple stream of magnetic stirring at room temperature (20–25 °C). The cold diazonium salt solution was added dropwise to the ethanolic mixture over a 10 min period while keeping the temperature in the range of 0–5 °C; on complete addition, reaction mixture was further stirred for 15 min at this temperature followed by gradual warming up to room temperature and another stirring for 30 min. Subsequently, the reaction flask was moved to

 

a refrigerator and left at 4 °C for 3 h to allow full precipitation. The obtained yellow-brown precipitate was filtered by vacuum on a Büchner funnel, successively washed with cold distilled water (3 × 50 mL) and then in cold ethanol (2 × 30 mL), followed by vacuum-drying at 50 °C during 4 h. The crude product was purified by recrystallization from a DMF/ethanol mixture (1 : 3 v/v, 80 mL total) to afford BHC as faint brown, fine crystals (4.15 g, 89% yield). Mp 273–275 °C (Lit. 271–273 (ref. 28)). FTIR (KBr) $\nu$ ($cm^{-1}$): 3267 (N–H), 1689 (C=O), 1632 (H–C=N). $^1$H NMR (400 MHz, DMSO-$d_6$) $\delta$ (ppm): 10.71 (s, 2H, 2 N–H), 7.88 (d, $J$ = 8.3 Hz, 4H, 4 Ar–H), 7.61 (d, $J$ = 8.2 Hz, 4H, 4 Ar–H), 2.39 (s, 6H, 2 $CH_3$). Full spectroscopic characterization data are provided in our previous study.[28]

**2.1.4. 1,1′-((Sulfonylbis(4,1-phenylene))bis(5-imino-4,5-dihydro-1,3,4-selenadiazole-4,2-diyl))-bis-(ethan-1-one) (BISDA).** Bis hydrazonoyl chloride (BHC, 0.466 g, 1.0 mmol) and potassium selenocyanate (KSeCN, 0.288 g, 2.0 mmol, 2.0 equiv.) were dissolved in a solvent mixture of absolute ethanol (20 mL) and anhydrous DMF (5 mL) in 100 mL round-bottom flask fitted with a magnetic stirrer and reflux condenser. The reaction mixture was stirred at room temperature (20–25 °C) for 10 min to give a homogeneous dispersion, resulting in a faint yellow solution. This with stirring and under nitrogen atmosphere for 3 h at reflux (oil bath temperature 85–90 °C), which was monitored by thin layer chromatography (TLC) on silica gel 60 $F_{254}$ plates [(dichloromethane/methanol (9 : 1 v/v))] where completion is marked by the disappearance of the BHC starting material spot ($R_f$ = 0.65) and a new single spot due to BISDA being observed ($R_f$ = 0.42). Upon the completion of the reaction, heating was stopped and the resultant mixture cooled to room temp with continuous stirring. Cold distilled water (50 mL) was then added dropwise over 5 min resulting in immediate precipitation of brown solid. The precipitate was isolated by vacuum filtration on a Büchner funnel, washed extensively with cold distilled water (3 × 30 mL), followed by cold ethanol (2 × 20 mL), and dried *in vacuo* at 60 °C for 6 h. The crude product was further purified *via* recrystallization from hot DMF/ethanol mixture (1 : 4 v/v, total volume 50 mL) to give BISDA as a brown microcrystalline powder (0.493 g, yield 83%). Mp > 300 °C (decomposes without melting). FTIR (KBr) $\nu$ ($cm^{-1}$): 3304 (N–H), 1688 (C=O), 1609 (C=NH), 1585 (C=N), 1324 ($SO_2$ asymmetric), 1153 ($SO_2$ symmetric), 736 (N–N), and 593 (C–Se–C). $^1$H NMR (400 MHz, DMSO-$d_6$) $\delta$ (ppm): 10.28 (s, 2H, 2 N–H), 7.88 (d, $J$ = 8.4 Hz, 4H, 4 Ar–H), 7.63 (d, $J$ = 8.5 Hz, 4H, selected Ar–H), $\delta$ ppm: pure and white compound was obtained after recrystallization from dioxane solvent. $^{13}$C NMR (151 MHz, DMSO-$d_6$) $\delta$ (ppm): 191.00, 158.37, 151.72, 143.13, 136.89, 128.49, 124.37, 25.95. Elemental analysis calcd for $C_{20}H_{16}N_6O_4SSe_2$ (594.37): C, 40.42; H, 2.71; N, 14.14%; found: C, 40.43; H, 2.72; N, 14.12%. BISDA was dissolved DMSO (1 mL, 100 μg $mL^{-1}$) to generate a stock solution for biological assays, briefly sonicated (5 s), and stored at −20 °C in aliquots until usage.

## 2.2. Biological assessment

**2.2.1. Culture of A549 cell line.** A549 cells were obtained from the American Type Culture Collection (cat. no. CCL-185, LGC Promochem, UK), served as a well-established and representative *in vitro* model for lung adenocarcinoma, facilitating direct comparisons with previous studies on novel anticancer agents. Cells were cultured in Dulbecco's modified Eagle's medium (DMEM) supplemented with 10% fetal bovine serum (FBS) and a 1% antibiotic mixture consisting of penicillin G sodium (10 000 IU), streptomycin (10 mg), and amphotericin B (25 μg) (all from Gibco, Thermo Fisher Scientific, Germany). Cells were incubated at 5% $CO_2$ and 37 °C. Following confluence, cells were detached using trypsin/EDTA (cat. no. 25200056, Gibco, Thermo Fisher Scientific, USA) for experimental purposes. All samples were analyzed in triplicate to ensure accuracy.

**2.2.2. Evaluating cytotoxic effect ($IC_{50}$) using MTT assay.** Twenty-four hours prior to the experiment, $8 \times 10^3$ cells per well were seeded and incubated in a sterile 96-well plate. Later, cells were treated and incubated with serial concentrations of the BISDA compound dissolved in the medium at the following concentrations: 0.01, 0.1, 1.0, 10, and 100 μg $mL^{-1}$ for 24 and 48 h. Untreated control A549 cells were incubated with 0.1% DMSO, and negative (cells treated with phosphate buffer saline; PBS) and positive (cells treated with 11.5 μg per mL cisplatin as a standard reference) control groups were also evaluated.

The tested compound was dissolved in DMSO to prepare a stock solution and subsequently diluted in culture medium to achieve final concentrations of 0.01–100 μg $mL^{-1}$. The final DMSO concentration did not exceed 0.1% (v/v) in any well. Untreated control cells were incubated with 0.1% DMSO in medium as vehicle control.

The cytotoxic effect ($IC_{50}$) of BISDA was evaluated using the MTT assay (Vybrant® MTT Cell Proliferation Assay Kit, Cat No. ≠M6494, ThermoFisher Scientific, Germany), a widely accepted colorimetric method for high-throughput screening of antiproliferative effects. Cell membrane integrity was further confirmed using the trypan blue exclusion method, alongside direct cell counts. In accordance with Hazekawa *et al.*,[29] the media were replaced with fresh media, and an MTT solution (1 mg $mL^{-1}$, Invitrogen, ThermoFisher Scientific, Germany) was added to each well at a volume of 20 μL for a 4-hour incubation. Following removal of the MTT solution, 100 μL of sodium dodecyl sulfate (SDS)-HCl was added to each well. Optical density was measured at 570 nm using an ELISA microplate reader (ELx 800; Bio-Tek Instruments Inc., Winooski, VT, USA). The $IC_{50}$ was calculated using the concentration–response curve and normalized to the negative control using GraphPad Prism software (version 9.1.0).

**2.2.3. Evaluating cell viability using trypan blue exclusion method.** Trypan blue was utilized for cell counting and viability assessments. Cells ($1 \times 10^4$ per well) were seeded in sterile 24-well plates for 24 h. Media were replaced with fresh media containing $IC_{50}$ concentration of BISDA compound. These two time points validated the cytotoxic results obtained from the $IC_{50}$ analysis. For non-attached cells, the medium containing floating cells was collected. For non-attached cells, medium with floating cells was collected. Attached cells were trypsinized with EDTA and resuspended in 1× Dulbecco's phosphate-buffered saline (DPBS, cat. no. ≠14190144, Gibco,

ThermoFisher Scientific, USA). The cell suspensions were mixed with 0.4% trypan blue dye 1 : 1 (cat. no. 15250061, Gibco, Thermo Fisher Scientific, USA) and incubated for 3 min at room temperature at RT. The mixture was examined using a hemocytometer and bright-field microscopy (LaboMed, USA).

**2.2.4. Evaluating cell apoptosis using Annexin V/PI staining.** Flow cytometry, utilizing Annexin V-FITC and propidium iodide (PI) double staining, was employed to assess the apoptotic activity of BISDA. This method differentiated between early and late apoptotic cells. Cells (1 × 10 cells per well) were seeded in sterile 6-well plates 24 h before the experiment. To investigate the mechanistic effects at a biologically relevant concentration, the cells were treated with BISDA $IC_{50}$ for 48 h, allowing for the observation of significant cellular responses while maintaining cell integrity for downstream assays. The cells were harvested and resuspended in annexin-binding buffer for 5 min at RT, stained with Annexin V/PI (Alexa Fluor® 488 annexin V/Dead cell apoptosis Kit, cat. no. ≠V13241, Invitrogen, ThermoFisher Scientific, UK) for 15 min at RT. Flow cytometry analysis was performed using a 488 nm argon-ion laser to measure fluorescence at 530 nm and 575 nm, as previously described.[30] Beckman Coulter Navios EX software (SM: BE14548 software version: Navios EX) was used to analyze the data.

**2.2.5. Evaluating cell cycle progression by flow cytometry.** Flow cytometry was used to determine the cell cycle arrest phases induced by BISDA. Both untreated and treated cells were initially fixed with cold methanol and subsequently stained with Vybrant DyeCycle Violet (cat. no. ≠V35003, Invitrogen, ThermoFisher Scientific, USA). The stained cells were then incubated at 37 °C for 30 min in darkness. Data acquisition was performed using a 405 nm excitation and 440 nm emission filter. Flow cytometry data were analyzed using Beckman Coulter Navios EX software (SM: BE14548, version Navios EX).

**2.2.6. Evaluating cell migration using transwell migration assay.** To assess the effect of BISDA on cell migration, a Transwell assay was performed. Briefly, untreated and treated cells (2 × $10^5$ cells per well) were resuspended in serum-free medium and seeded into the upper chambers of cell culture inserts (Thermo Scientific™ Nunc™, cat. no. ≠140629, ThermoFisher Scientific, USA). Complete DMEM was added to each well of the lower chamber of the insert. The cells were then incubated at 37 °C for 24 h. Cells that migrated to the lower surface of the insert membrane were fixed with 4% paraformaldehyde (PFA) (cat. no. ≠P6148, Sigma-Aldrich, Germany) for 15 min. and stained with 0.1% crystal violet (cat. no. ≠C0775; Sigma-Aldrich). The number of migrated cells was imaged at 20× magnification using an inverted microscope (Labomed, USA) and a Vega Digital Camera. At least five images from each sample were captured and analyzed using the ImageJ software (version 1.53, National Institutes of Health, Bethesda, MD, USA). All the settings were adjusted to calculate the total number of migrated cells per field.

**2.2.7. Evaluating endogenous antioxidant status.** Glutathione peroxidase (GPx) and glutathione (GSH) activity were evaluated to determine the possible effects of BISDA on the oxidative stress status and antioxidant response of A549 cells. Cells (1 × $10^6$) from untreated and treated cells were homogenized in PBS (0.01 M, pH 7.4) at 4 °C and then centrifuged at 10 000×*g* for 10 min. The supernatant was separated and stored on ice for subsequent analysis. GSH-Px activity was measured using a GSH-Px activity assay kit (cat. no. ≠E-BC-K096-S; Elabscience Biotechnology, USA) and reduced glutathione (cat. no. ≠E-BC-K030-M), following the manufacturer's instructions, and read at OD 412 nm using an ELISA microplate reader (DIALAB Diagnostics, Neudorf, Austria).

**2.2.8. Immunofluorescence (IF) staining.** The expression of programmed cell death protein 1 (PD-1) and interferon-γ (IFN-γ), both involved in immunomodulatory pathways, was quantified using immunofluorescence (IF) staining. Untreated and treated cells were fixed with 4% paraformaldehyde (PFA) and blocked with blocking serum to minimize background staining. Subsequently, cells were incubated overnight at 4 °C with primary antibodies–PD-1 Polyclonal Antibody (cat. no. #PA5-20351 and IFN-γ Monoclonal Antibody, cat. no. #MA5-44024, Invitrogen, ThermoFisher Scientific, USA) diluted 1 : 400 overnight at 4 °C. The following day, cells were washed with phosphate-buffered saline (PBS) and then incubated with Alexa Fluor 488 secondary antibodies (Goat anti-rabbit for PD-1 and anti-mouse for IFN-γ), diluted at 1 : 100, from Invitrogen, ThermoFisher Scientific, Hilden, Germany. Slides were counterstained with DAPI (Prolong Gold Antifade DAPI counter stain Reagent (10 μg $mL^{-1}$), Abcam, Cambridge, UK) and mounted overnight at room temperature (RT). Imaging was conducted using a fluorescence microscope (LABOMED LX400, USA). IF staining intensity was assessed using a four-tier scoring system, and the median H-score was calculated according to.[31]

**2.2.9. Quantitative gene expression analysis RT-qPCR.** The gene expression of the epidermal growth factor receptor (EGFR) and genes related to its downstream pathways was investigated using quantitative PCR in untreated and treated cells. 1 × $10^6$ cells were homogenized and lysis was carried out in a guanidine–thiocyanate–containing buffer.[32] Total RNA was extracted and purified using RNeasy Mini Kit (cat. no. 74104; Qiagen, Hilden, Germany) following the manufacturer's instructions. RNA was then used in a cDNA synthesis reaction employing the QuantiTect Reverse Transcription Kit (cat. no. ≠205310, Qiagen, Hilden, Germany), according to the manufacturer's instructions. Gene expression was measured using the QuantiTect primer assay (Table 1) and QuantiTect SYBR Green PCR Kit (Qiagen, Germany) with a 5 Rotplex or Gene PCR Analyzer (Qiagen, Germany). All genes were normalized to the β-actin housekeeping gene. The relative mRNA expression (*i.e.*, fold change) for each gene was calculated using the $2^{(-\Delta\Delta Ct)}$ equation.[33]

$$\Delta Ct(\text{tested} = Ct(\text{target in the teste groups}) - Ct(\text{ref. in test group})$$

$$\Delta Ct(\text{calibrator}) = Ct(\text{target in control}) - Ct(\text{ref. in control})$$

$$\Delta\Delta Ct = C\Delta\ Ct(\text{test}) - \Delta Ct(\text{calibrator})$$

$$\text{Fold change} = 2^{(-\Delta\Delta Ct)}$$

Table 1 Primers used for amplification

| | Gene | Assay name | Assay ID |
|---|---|---|---|
| 1 | Epidermal growth factor receptor (EGFR) | Hs_EGFR_1_SG QuantiTect primer assay | QT00085701 |
| 2 | Protein kinase B (Akt) | Hs_AKT1_1_SG QuantiTect primer assay | QT00085379 |
| 3 | Mitogen-activated protein kinase 1 (MAPK1) | HS_MAPK3_2_SG, QuantiTect primer assay | QT02589314 |
| 4 | Mechanistic target of rapamycin (MTOR) | Hs_MTOR_1_SG QuantiTect primer assay | QT00056133 |
| 5 | Transforming growth factor-beta (TGFB) | HS_TGFBRAP1_1_SG QuantiTect primer assay | QT00057155 |
| 6 | Heat shock protein 60 (HSP 60) | Hsp60 (HSPD1) | NM_002156 |
| 7 | Heat shock protein 70 (HSP70) | HSP70-1A | NM_005345 |
| 8 | Heat shock protein 90 (HSP 90) | Hs_HSP90B2P_1_SG QuantiTect primer assay | QT01152550 |

**2.2.10. ADMET methodology.** The absorption, distribution, metabolism, excretion, and toxicity (ADMET) profile of the investigated compound was evaluated using the pkCSM web server, a graph-based signature modeling platform for pharmacokinetic and toxicity prediction. Predictions were performed using the canonical SMILES representation of the ligand under study. pkCSM employs validated machine learning models trained on large experimental datasets to estimate pharmacokinetic behavior and toxicity endpoints relevant to drug development. All predictions were generated under default settings.

**2.2.11. Statistical analysis.** All experiments were conducted in triplicate, and data are presented as mean ± standard error of the mean (SEM). Statistical comparisons were performed using one-way analysis of variance (ANOVA) followed by Tukey's *post hoc* test using GraphPad Prism (version 8.0.1). A $p$-value < 0.05 was considered statistically significant. Significance levels were defined as $p < 0.05$; *$p < 0.01$; **$p < 0.001$; ****$p < 0.0001$; ns = not significant.

# 3 Results and discussion

## 3.1. Synthesis protocol

Hydrazonoyl halides are versatile precursors for the synthesis of heterocyclic derivatives. Selenadiazoles are unique selenium-containing heterocycles characterized by a five-membered ring composed of two nitrogen atoms and one selenium atom. This study focused on the preparation of novel selenadiazole derivatives. The reaction of hydrazonoyl halides with potassium selenocyanate has been previously reported.[34] Specifically, the reaction of bishydrazonoyl chloride (BHC) with potassium selenocyanate under reflux conditions yielded a novel S-alkylated intermediate, which subsequently underwent *in situ* cyclization under the same conditions to afford the corresponding bisselenadiazolimine (BISDA) derivative (Scheme 1). This process consistently produced a single isolable product (BISDA), confirmed *via* thin-layer chromatography (TLC). The formation of the final products was explained through a mechanism involving nucleophilic attack of the thiocyanate anion, followed by intramolecular cycloaddition. BISDA was obtained in high purity and good yield, and its molecular structure was elucidated using microanalysis and spectral data.

## 3.2. FTIR spectroscopy

The FTIR spectrum of BISDA agrees with the bis (1,3,4-selenadiazole) structure, along with sulfonyl-bridged aryl and acyl substituents, including all characteristic functional groups such as imino, carbonyl, sulfonyl, and selenadiazole rings. The lack of impurity bands and well-resolved diagnostic absorptions indicate the successful synthesis of a single molecular species.[35] For example, the medium sharp band, 3304 $cm^{-1}$, corresponds to N–H stretching vibration that supports the imino/amine functionality coming from the 5-imino-4,5-dihydro-1,3,4-selenadiazole.[36] A strong absorption peak at 1688 $cm^{-1}$ is assigned to the carbonyl stretching of ethanone units attached to selenadiazole ring. The blue shift of this C=O band indicated its conjugation with the heteroaromatic system, which weakened the C=O bond. Two bands at 1609 and 1585 $cm^{-1}$ are assigned to C=NH and C=N stretching vibrations, the presence of which confirms the existence of the 1,3,4-selenadiazole core and imino substitution at C-5. Such vibrations favor the formation of heterocycles over open-chain diazines or hydrazine byproducts.[37] The sulfonyl linker was confirmed by asymmetric $SO_2$ and symmetric $SO_2$ stretching vibrations at 1324 and 1153 $cm^{-1}$, respectively, imparting the aryl sulfone moiety.[38] The band at 736 $cm^{-1}$ is due to N–N stretching in the 1,3,4-selenadiazole system, which is characteristic of such heterocycles. The band at 593 $cm^{-1}$ is due to the vibration of C–Se–C, indicating the incorporation of Se into the heteroaromatic system.

Interestingly, the presence of powerful electron-withdrawing ($SO_2$, C=O) and delocalized/charge-rich electron-donating centers (C=NH, C=N, Se) in a rigid π-conjugated skeleton implies strong intramolecular charge transfer processes and multiple metal ion/biomolecule binding sites.[39] This combination is exciting for organoselenium materials, redox-active ligands, or bioactive heterocycles, and FTIR data assist in supporting such structure–property discussions.

## 3.3. NMR spectroscopy

The $^1H$ and $^{13}C$ NMR spectra of BISDA are consistent with the proposed structure of 1,1′-((sulfonylbis(4,1-phenylene))bis(5-imino-4,5-dihydro-1,3,4-selenadiazole-4,2-diyl))bis (ethan-1-one) and corroborate the FTIR assignment of a symmetric sulfonyl-bonded bis-selenadiazolimine scaffold. The spectra exhibited only one symmetrical species in solution without

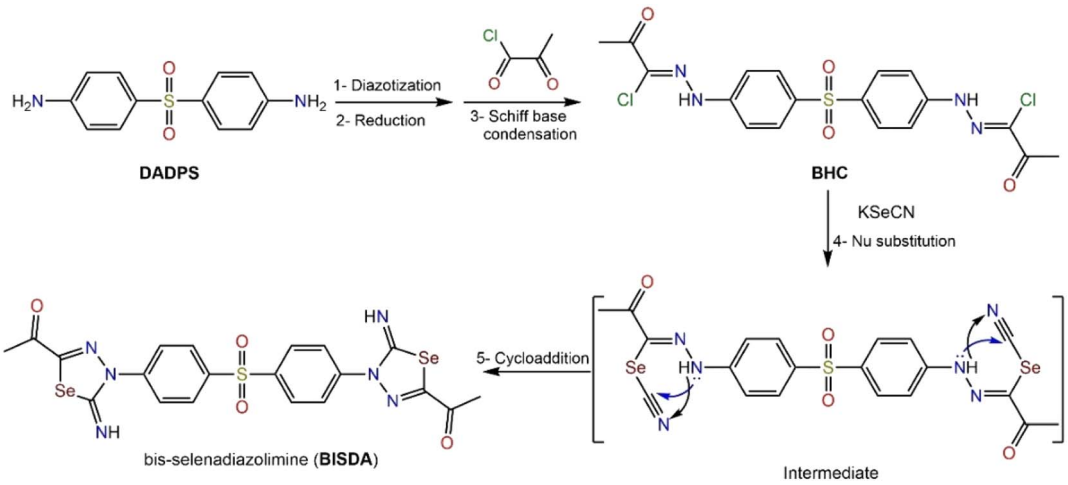


Scheme 1 Synthesis of bis-selenadiazolimine (BISDA) derivatives.

resonances for the starting materials, regioisomers, and decomposition products.

In the $^1$H NMR spectrum (Fig. 1), a singlet at $\delta(H) = 10.28$ for two protons is ascribed to the equivalent N–H groups of the imino units at position 5 of each 1,3,4-selenadiazole ring. The high chemical shift and singlet of the above signal can be ascribed to non-exchange broadened imino/amide-like protons in the vicinity of the electron-withdrawing carbonyl groups and heteroaryl moieties in a rigid environment. Two aromatic doublets at 7.88 ppm (4H, $J = 8.4$ Hz) and 7.63 ppm (4H, $J = 8.5$ Hz) arise from the *para*-disubstituted phenylene rings over the sulfonyl bridge. The identical integration and similar coupling constants underscore the symmetric AA′BB′ pattern on the 1,4-disubstituted aromatic rings, in agreement with the sulfonyl-bis(4,1-phenylene) core.[40] A singlet at 2.20 ppm with six proton integration results was assigned to the two equivalent methyl groups of the ethanone (–CO–$CH_3$) moieties in the selenadiazole units. No further aliphatic resonances suggested two chemically equivalent methyl sites, ruling out residual *N*-alkylated side products or partially functionalized intermediates.

The $^{13}$C NMR spectrum (Fig. 2) displays a resonance at 25.12 ppm corresponding to the methyl carbons of acetyl group, indicative of deshielded aliphatic carbons bearing a conjugated carbonyl moiety. The multiplet at 191.82 ppm is characteristic of a conjugated ketonic carbonyl, displaying two equivalent –CO–$CH_3$ functionalities in the – π-extended heteroaryl–aryl context. Several peaks in the range of 124.37–158.37 ppm are assigned to aromatic and heteroaromatic carbons (phenylene rings, 1,3,4 selenadiazole cores). The chemical shifts at 158.37 and 151.72 ppm are due to the C=N/C=NH type carbon, whereas the resonances at 143.13 and 136.89 ppm can be

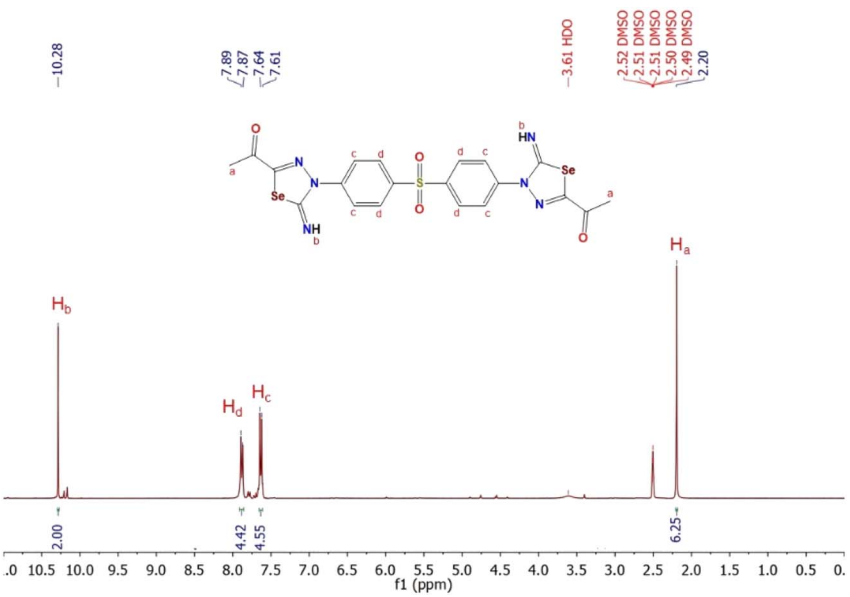


Fig. 1 $^1$H NMR spectrum of bis-selenadiazolimine (BISDA).

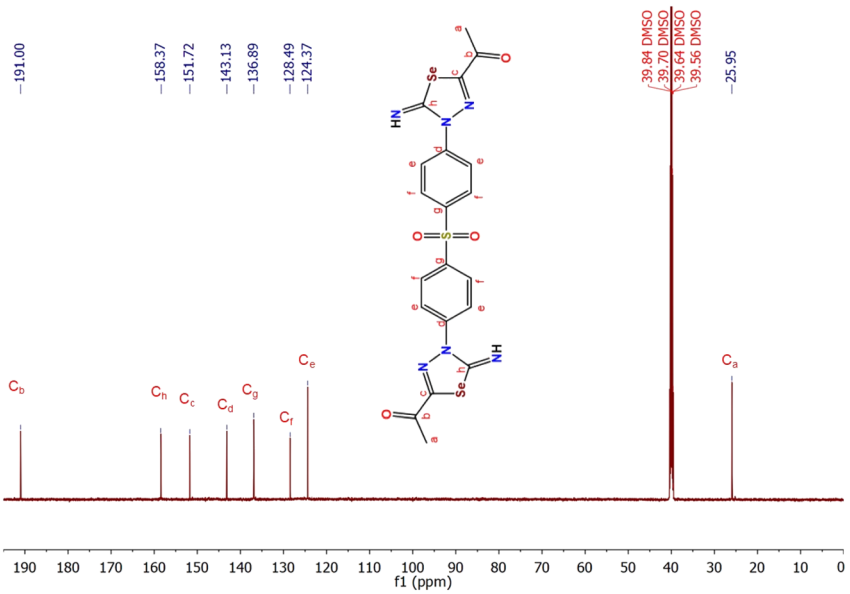


Fig. 2 $^{13}$C NMR spectrum of bis-selenadiazolimine (BISDA).

attributed to ipso and quaternary aromatic carbon with sulfonyl and heteroaryl substitutes.[41] The peaks at 128.49 and 124.37 ppm are the aromatic CH carbons of *para*-disubstituted phenylene rings, suggesting that this molecule has high molecular symmetry. The observation of only eight non-equivalent carbon resonances, despite molecular complexity, corresponds to two symmetric-related halves and equivalent rings, which confirms the centrosymmetric bis selenadiazolimine structure.

Overall, the $^{1}$H and $^{13}$C NMR data collectively corroborate a rigid, $C_2$-symmetric bis-heteroaryl core in which two imino-functionalized 1,3,4-selenadiazole rings are connected *via* a sulfonyl-bridged *para*-phenylene linker and terminally functionalized by acetyl substituents. The field N–H signal, conjugated carbonyl carbon, and de-shielding C=N/C=NH carbons provide evidence of the strong electron-withdrawing power of the sulfonyl and carbonyl groups, as well as the extended conjugation along the aryl–selenadiazole–carbonyl axis.

### 3.4. Selenadiazole derivative BISDA cytotoxicity $IC_{50}$ values *via* MTT assay and trypan blue

To further assess the selectivity of BISDA toward malignant cells, its cytotoxic effect was evaluated in parallel on the human normal bronchial epithelial cell line BEAS-2B and the A549 lung adenocarcinoma cell line under identical conditions (serial concentrations over 24 or 48 h). Concentration–response analysis revealed that the $IC_{50}$ for BISDA was significantly greater in BEAS-2B cells (60.73 μg mL$^{-1}$ after 24 h) than A549 cells, where the $IC_{50}$ values were lower at 15.62 μg mL$^{-1}$ and 2.609 μg mL$^{-1}$ after exposure to BISDA for 24 h or 48 h, respectively (Fig. 3A–C). This differential suggests that normal bronchial epithelial cells are tolerant to significantly higher concentrations of BISDA than A549 cancer cells, which is conducive to a beneficial therapeutic window. In line with these $IC_{50}$ values, viability curves revealed a more pronounced and time-dependent decrease in A549 cell survival within the tested concentration range (0.01–100 μg mL$^{-1}$) but much higher viabilities of BEAS-2B cells at respective doses. Collectively, these findings indicate that BISDA specifically inhibits the growth of lung cancer cells and has a lower toxicity towards normal bronchial epithelial cells, supporting its further consideration as an anticancer drug candidate. Cells treated with an $IC_{50}$ concentration of 2.609 μg mL$^{-1}$ for 48 h (treated group) were compared to cells treated with 0.1% DMSO for 48 h (untreated group). The compound exhibited a concentration-dependent impact on cell viability at both intervals, with notable effects observed at 1 μg mL$^{-1}$ when compared to the control group ($p < 0.001$ for 24 h and $p < 0.0001$ for 48 h) (Fig. 3D). In comparison to cisplatin, the novel synthesized compound at 100 μg mL$^{-1}$ showed similar cell toxicity to the positive control (11.5 μg mL$^{-1}$) after 24 h, with no significant difference ($p > 0.05$; Fig. 3D) offering greater safety than cisplatin at elevated concentrations. Comparing the time intervals, the results showed that incubation time had no significant effect ($p > 0.05$) on the cell viability percentage at all concentrations, except at 1 μg mL$^{-1}$ which was significantly different between 24 and 48 h ($p < 0.0001$, Fig. 3D).

Furthermore, the trypan blue exclusion method revealed a significant reduction in the percentage of viable cells in the treated group compared to the untreated group ($p < 0.0001$, Fig. 4A–C), demonstrating the potent cytotoxic effects of the BISDA compound as an anticancer agent.

The results from the MTT and trypan blue assays demonstrated the antiproliferative effects of the BISDA compound, which contains a variety of bioactive components, including sulfone, selenadiazole, imino, and ketone aromatic ring compounds. These findings align with previous research indicating that numerous sulfone derivatives exhibit significant cytotoxic and antiproliferative effects on LUAD A549 cells,[42]

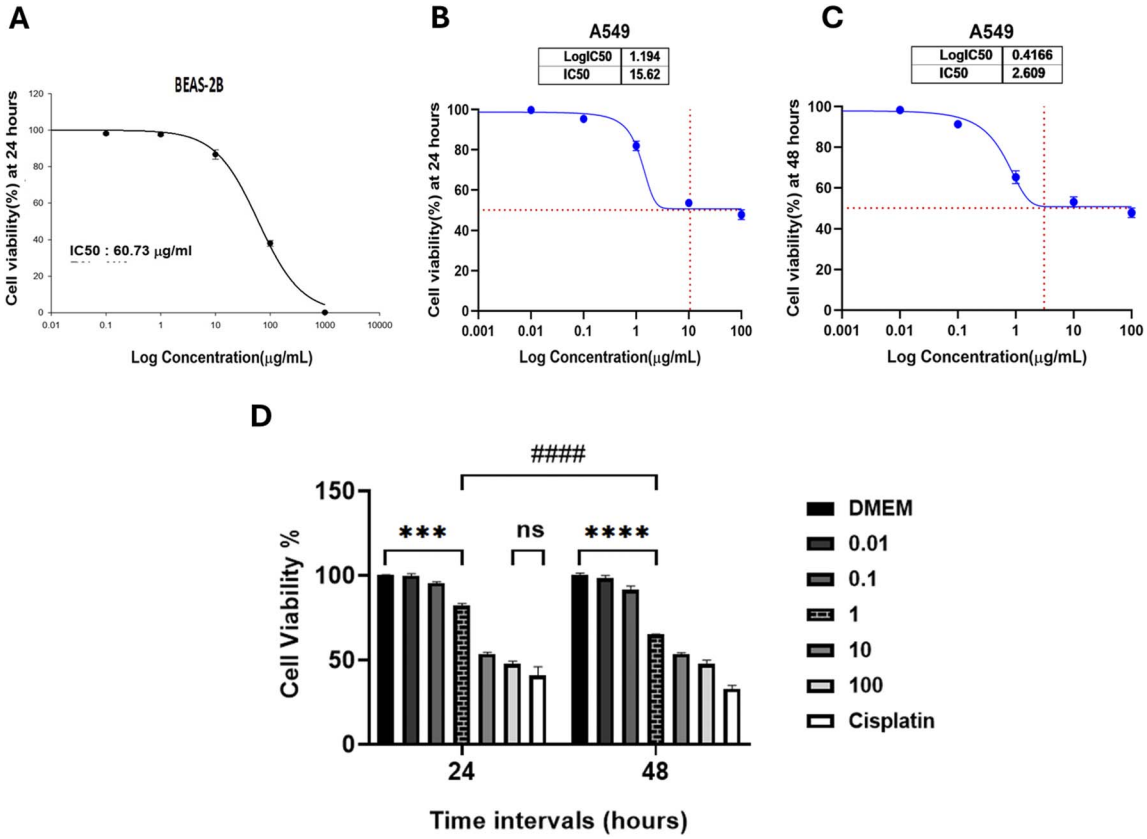


Fig. 3 The half-maximal inhibitory concentration ($IC_{50}$) of BISDA compound on the BEAS-2B normal cell line and the A549 cancer cell line at various concentrations, incubated for 24 or 48 h. The concentration response curve defined the $IC_{50}$ after incubation for 24 h for BEAS-2B normal cell line (A), after 24 h (B) and after 48 h (C) for A549 cancer cell line. (D) Percentage of cell viability after 24 and 48 h of incubation with different concentrations (0.01, 0.1, 1.0, 10, and 100 µg $mL^{-1}$). No treatment (*i.e.* DMEM group) was used as the negative control group. Cisplatin (11.5 µg $mL^{-1}$) was used as a positive control group. ***$p < 0.001$, ****$p < 0.0001$ indicate differences between different concentrations at specific time interval. $^{\#\#\#\#}p < 0.0001$ indicates differences between the two-time intervals ns: non-significant. Data are presented as the mean ± SEM, $n = 3$ in each condition.

leukemia cell lines,[10] and head and neck squamous cell carcinoma.[11] Furthermore, selenadiazole, ketone aromatic ring (chalcones), and imino derivatives displayed enhanced cytotoxicity in multiple cell lines, including LUAD PC9, gastric cancer SGC7901,[12] liver cancer HCT116,[14] breast cancer MCF7 (ref. 43) and colon cancer HT29.[44]

### 3.5. The activity of the BISDA compound on the antioxidant system

Treatment of A549 LUAD cells with BISDA altered the antioxidant profile. Glutathione peroxidase (GPx) activity decreased from 22 U per mg protein to 12 U per mg protein with BISDA treatment ($p < 0.01$). This reduction suggests elevated oxygen free radicals (ROS) levels due to diminished hydroperoxide reduction. This inhibition aligns with the pro-oxidant mechanisms of organoselenium compounds in cancer cells.[45] Conversely, the levels of reduced glutathione (GSH) increased from 13 nmol per mg protein in untreated cells to 25 nmol per mg protein in treated cells ($p < 0.01$). This increase in GSH levels indicates cellular adaptation to oxidative stress resulting from reduced GPx function. This redox imbalance, with decreased GPx activity despite higher GSH levels (Fig. 5A and B), led to peroxide accumulation and subsequent apoptosis of A549 cells (Fig. 4C and 6C). This disruption underlies the inhibition of cell proliferation by the compound (Fig. 4C) and the modulation of EGFR/AKT/mTOR/HSP networks, suggesting that selenadiazole derivatives (BISDA) interacts with GPx to induce ROS, whereas the selenium center offers partial compensation. These findings demonstrate that BISDA disrupts redox homeostasis by suppressing GPx activity and triggering GSH upregulation, which is consistent with the prooxidant mechanisms of selenadiazoles. This perturbation demonstrated the inhibitory activity of the compound on cell proliferation (Fig. 4C) and the modulation of EGFR/AKT/mTOR/HSP networks.

The imbalance in redox reactions hinders peroxide removal, intensifying pro-oxidant conditions and leading to apoptosis. This observation aligns with seleno compound research, where increased glutathione (GSH) is an inadequate response to oxidative stress.[46] This is attributed to the GPx-mimetic properties of selenadiazole, which partially offsets endogenous GPx loss. This behavior is typical of organoselenium compounds.[47] BISDA showed antiproliferative properties by inhibiting GPx

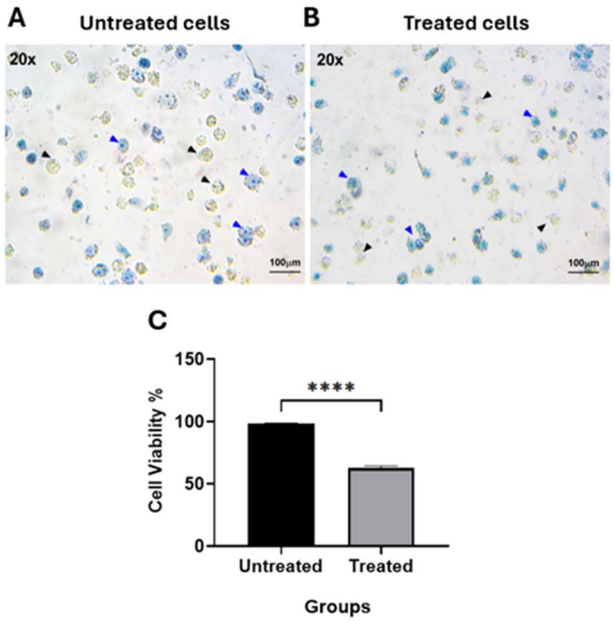


Fig. 4 Trypan blue exclusion method of A549 cell line after treatment with the determined $IC_{50}$ (2.609 µg $mL^{-1}$) for 48 h. Representative photomicrographs of untreated (0.1% DMSO) (A) and treated (B) groups stained with trypan blue dye. Black arrows indicate viable cells, which appear clear and unstained, whereas blue arrows indicate dead cells, which exhibit blue cytoplasmic staining. Images were captured at 20× magnification. Scale bars, 100 µm. (C) Percentage (%) of viable cells in the untreated and treated groups. ****$p < 0.0001$ indicates differences between untreated and treated groups. Data are presented as the mean ± SEM, $n = 3$ in each condition.

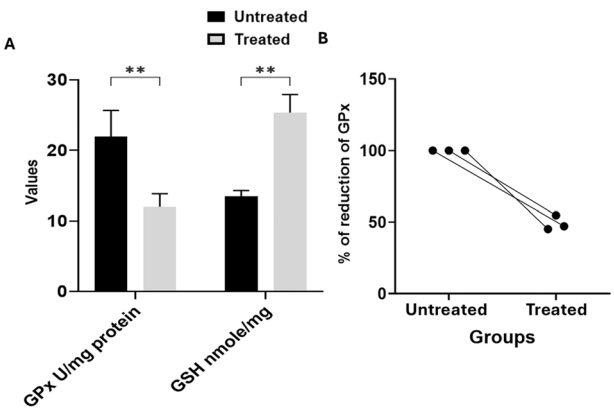


Fig. 5 Effect of BISDA on the antioxidant system in the A549 cell line after treatment with the determined $IC_{50}$ (2.609 µg $mL^{-1}$) for 48 h. (A) Glutathione peroxidase (U per mg protein) and glutathione (nmol per mg protein) in untreated and treated groups. (B) Glutathione peroxidase reduction percentages (%) in the untreated and treated groups. **$p < 0.01$ indicates differences between the untreated and treated groups. Data are presented as mean ± SEM, $n = 3$ in each condition. GPx: glutathione peroxidase. GSH: glutathione.

and generating ROS while providing mimetic support through its selenium component. This modulation disrupts antioxidant defenses, targeting oncogenic pathways such as EGFR/AKT/mTOR/HSP networks, making BISDA promising for redox-targeted strategies in non-small cell lung cancer (NSCLC) models.[48] Therefore, the observation that BISDA, a selenium-containing compound, inhibits GPx – a selenoenzyme with antioxidant function – exemplifies the "selenium paradox" in cancer biology. Selenium exhibited a remarkable dose-dependent duality.

Cancer cells exhibit alterations in thiol metabolism, particularly glutathione (GSH), the primary non-protein thiol antioxidant within cells. GSH maintains redox balance by neutralizing reactive oxygen species (ROS) and mitigating oxidative stress, which is exacerbated by rapid growth, altered metabolism, and oncogenic signaling. Consequently, many cancer cells increase GSH levels and associated pathways to counteract elevated ROS production and reduce sensitivity to chemotherapy and radiotherapy. This pattern is observed across diverse cancers, including breast, colon, lung, melanoma, and others.[49]

In contrast, organoselenium compounds deplete glutathione (GSH) more effectively in cancer cells, which rely on GSH for redox balance.[50] Furthermore, methylselenol increased GSH levels in normal cells and decreased GSH levels in malignant cells, resulting in cytotoxicity. This dual mechanism may enhance the therapeutic window for selenium compounds.[51]

### 3.6. Effects of BISDA compound on cell apoptosis and cell cycle progression

Flow cytometry was employed to examine Annexin V/PI staining and assess the apoptotic effects of BISDA. Cells treated with 2.609 µg $mL^{-1}$ of BISDA for 48 h exhibited significant apoptotic effects. The compound increased early apoptosis to 51.7% ± 0.2 and late apoptosis to 3.6% ± 0.03, compared with 0.95% ± 0.03 and 0.55% ± 0.03 in the untreated group ($p < 0.0001$ for both early and late apoptotic induction) (Fig. 6A–C).

Flow cytometry was also employed to identify potential arrest phases induced by the BISDA compound. The results revealed that in the untreated group, the percentages of cell populations in the S phase and G2/M phase were 27.5% ± 0.5 and 69.9% ± 0.7, respectively. Following treatment with 2.609 µg per mL BISDA for 48 h, these percentages decreased to 5.8% ± 0.2 ($p < 0.0001$) and 93.5% ± 1.2 ($p < 0.0001$) in the S phase and G2/M phase, respectively (Fig. 7A–C). Simultaneously, the increased G2/M phase indicates that BISDA may trigger DNA damage, leading to G2/M arrest for repair before mitosis, or cell accumulation prior to apoptosis if repair is unsuccessful.[52] Meanwhile, the increased G2/M phase confirms that the BISAD compound may trigger DNA damage leading to G2/M arrest for repair before mitosis or cell accumulation before apoptosis if repair fails.[53]

The flow cytometry results demonstrated that BISDA exhibited strong apoptotic effects (Fig. 6A–C) and inhibited cell cycle progression in the cancerous A549 cell line by inducing cell cycle arrest (Fig. 7A–C). Previously, sulfone, ketone aromatic ring, and selenadiazole derivatives, three of the bioactive components in our synthetic compound, were shown to induce apoptosis in the lung,[12,42] liver[54] and cervical[8] cancer cells by increasing the production of reactive oxygen species (ROS), inducing mitochondrial apoptosis *via* activation of three JAK2/

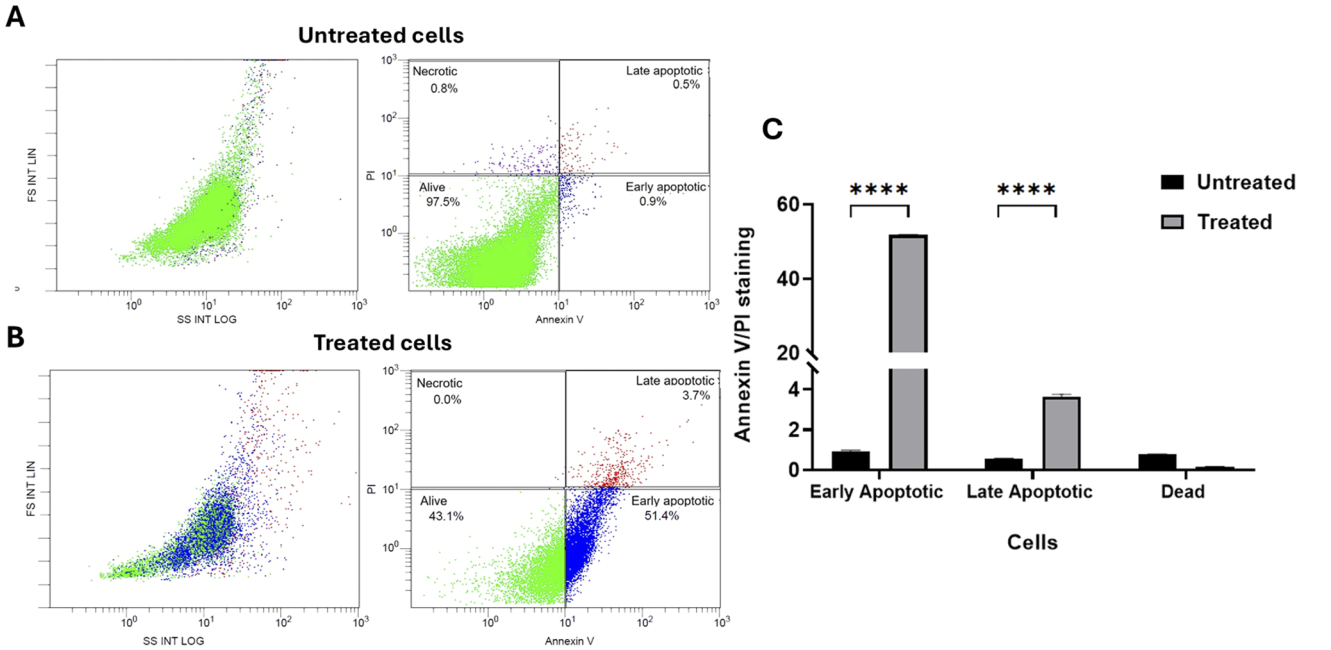


Fig. 6 Apoptotic effects of BISDA compound on A549 cell line after treatment with the determined $IC_{50}$ (2.609 μg $mL^{-1}$) for 48 h using flow cytometry. Representative flow cytometry plots of Annexin V for untreated (A) and treated (B) cells show the percentage of late apoptotic, early apoptotic, and dead cells. (C) Quantitative analysis of annexin V/PI-positive cells in untreated and treated groups. ****$p < 0.0001$ indicates differences between the untreated and treated groups. Data are presented as mean ± SEM, $n = 3$ in each condition.

STAT3 pathway, activating ferroptosis stimulating the pro-apoptotic caspase pathway, and inhibiting the formation of lactate in glucose metabolism. Thus, the elevated levels of Annexin V/IP observed in the current study (Fig. 6A–C) could also reflect the activation of mitochondrial apoptosis, confirming the apoptotic effect of BISDA.[8] Plano *et al.*,[44] Ji *et al.*,[55] and Appalanaidu *et al.*[15] reported that selenadiazole, ketonerings, g, and imino derivatives inhibited cell cycle progression by inducing G2/M cell cycle arrest in breast cancer, bone cancer, and melanoma cell lines, respectively. In agreement with previous studies, our results showed the same observation of G2/M arrest (Fig. 7A–C) after treatment with BISDA, which contains the same bioactive compounds.

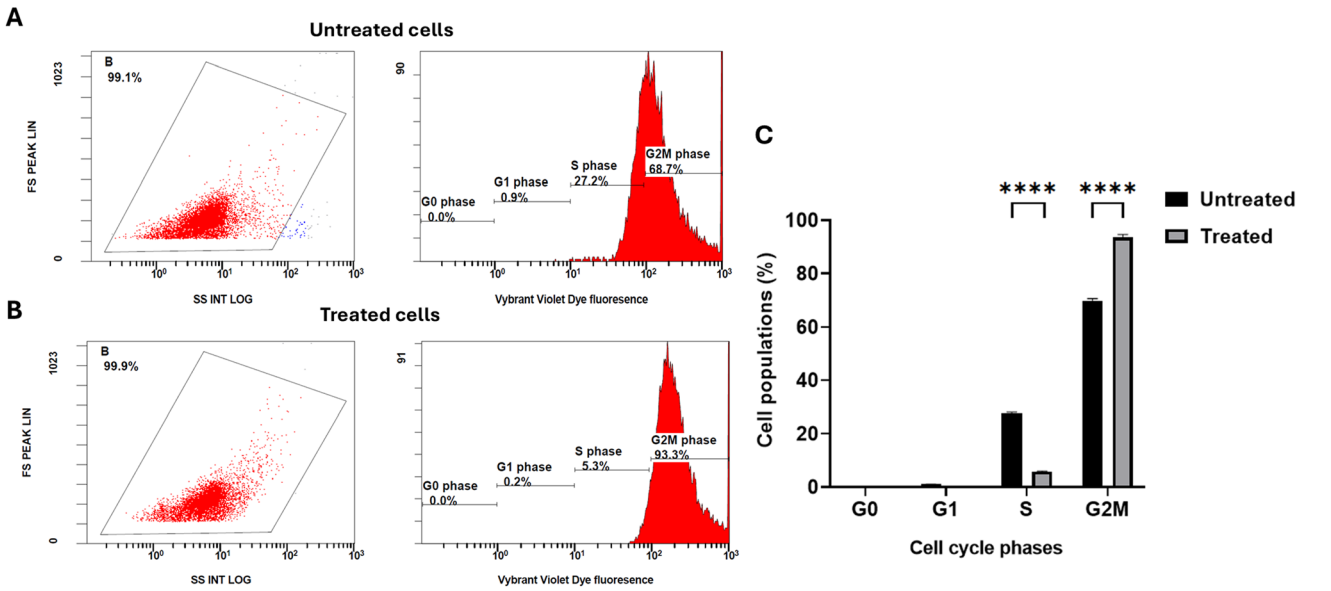


Fig. 7 Effects of BISDA compound on A549 cell line cell cycle progression after treatment with the determined $IC_{50}$ (2.609 μg $mL^{-1}$) for 48 h using flow cytometry. Representative flow cytometry plots of Vybrant Violet Dye stain for the untreated (A) and treated (B) groups. (C) Percentage of cell populations in cell cycle phases in the untreated and treated groups. ****$p < 0.0001$ indicates differences between the untreated and treated groups. Data are presented as mean ± SEM, $n = 3$ in each condition.

### 3.7. Effects of BISDA compound on cell migration

Cell migration is a prominent characteristic of cancer cells and is indicative of cancer metastasis.[56] Transwell migration assay showed that BISDA significantly inhibited the migration of cancerous A549 cells, leading to a 50% reduction in relative migration compared to controls ($p < 0.001$, Fig. 8A–C). Imino derivatives can compete with enzymes crucial for cancer metastasis (*e.g.*, glycosidases) and inhibit their activity.[16] This observation may explain the reduction in relative migration observed following BISDA treatment. The apoptotic and S phase-halting activities of the synthesized compound are dependent on the sulfone group (R–$SO_2$–R′), which imparts unique properties to aromatic compounds.[57] The electron-withdrawing effects of the sulfonyl moiety alter the electron density of the aromatic system, influencing interactions with nucleophilic sites on biological macromolecules, including cysteine residues and DNA nucleobases.[58] Furthermore, the lipophilicity of sulfone-containing aromatics facilitates hydrogen bond acceptance and enhances protein binding. Selenadiazole groups exhibit antitumor potential against cancers by inducing apoptosis, reducing cell viability, and modulating ROS-mediated DNA damage and signaling pathways.[59,60]

According to Islam *et al.*,[61] the PI3K/AKT signaling pathway plays a crucial role in promoting cancer cell migration and invasion. This pathway has been targeted to inhibit various forms of cancer metastasis.[61] The reduction in AKT1 expression (Fig. 10A) and decreased migration of A549 cells (Fig. 8A–C) following BISDA treatment indicated the potential antimetastatic properties of the compound as an anticancer agent. Additionally, transforming growth factor-β (TGF-β) cytokines, which regulate cell cycle progression and differentiation,[62] were significantly reduced in BISDA-treated A549 cells compared with those in the untreated group, with a decrease of $p < 0.0001$ (Fig. 10A), thus supporting its antimetastatic properties.

### 3.8. Effects of BISDA compound on programmed cell death protein 1 (PD1) and interferon-gamma (IFN-γ)

Programmed cell death protein 1 (PD-1) and interferon-gamma (IFN-γ) are crucial proteins involved in immunomodulatory pathways and serve as cancer biomarkers, reflecting the efficacy of anticancer treatments.[21,63] Following treatment with 2.609 μg per mL BISDA for 48 h, A549 cells exhibited significant upregulation of PD-1 protein expression relative to the untreated group ($p < 0.0001$, Fig. 9A and C). Conversely, treated A549 cells demonstrated a significant decrease in IFN-γ expression compared to the untreated group ($p < 0.0001$, Fig. 9B and C). IFN-γ has been reported to play a crucial role in tumor progression through anti-apoptotic and metastatic effects.[64,65] Consistent with our results, BISDA inhibited IFN-γ in A549 cell lines, suggesting its ability to repress tumor progression and trigger apoptosis, as confirmed by a 50% reduction in relative migration (Fig. 8A–C) and an increase in Annexin V/PI and apoptotic cell populations (Fig. 6A–C) in the treated group compared to the untreated group.

This observation distinguishes PD1 upregulation from IFN-γ signaling, suggesting a stress-responsive pathway independent of cytokine-driven transcription.[66,67] Cancer cell behavior may induce increased PD1 expression in response to stress induced by BISDA. These results support the combined use of BISDA with PD1/PD-L 1 checkpoint inhibitors to enhance cytotoxic effects and disrupt survival signals, potentially boosting antitumor activity in A549 cells.

### 3.9. Effects of BISDA compound on different relative gene expressions

The relative expression of EGFR and other genes related to its downstream pathways, as well as other genes involved in tumor progression, was investigated using quantitative PCR. The results demonstrated that treatment of A549 cells with 2.609 μg per mL BISDA for 48 h downregulated the relative expression of all investigated genes compared to the untreated group; however, only *TGF-β* ($p < 0.0001$), *AKT1* ($p < 0.05$), *HSP60* ($p < 0.001$), *HSP70* ($p < 0.0001$), and *HSP90* ($p < 0.0001$) exhibited statistically significant differences (Fig. 10A). Heat shock proteins (HSPs) are a group of highly conserved molecular chaperones that are essential for maintaining protein balance and responding to cellular stress. The current use of BISDA in LUAD demonstrates inhibitory effects on HSP60, HSP70, and

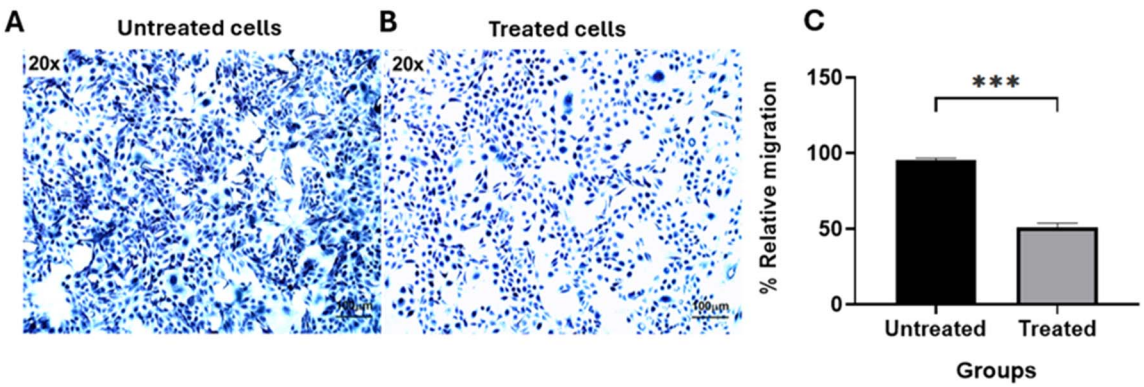


Fig. 8 Cell migration of A549 cell line after treatment with the determined $IC_{50}$ (2.609 μg $mL^{-1}$) for 48 h using Transwell migration assay. Representative photomicrographs of untreated (A) and treated (B) groups stained with 0.1% crystal violet. Images were captured at 20× magnification. Scale bars, 100 μm. (C) Percentage (%) of relative migration in the untreated and treated groups. ***$p < 0.001$ indicates differences between untreated and treated groups. Data are presented as mean ± SEM, $n = 3$ in each condition.

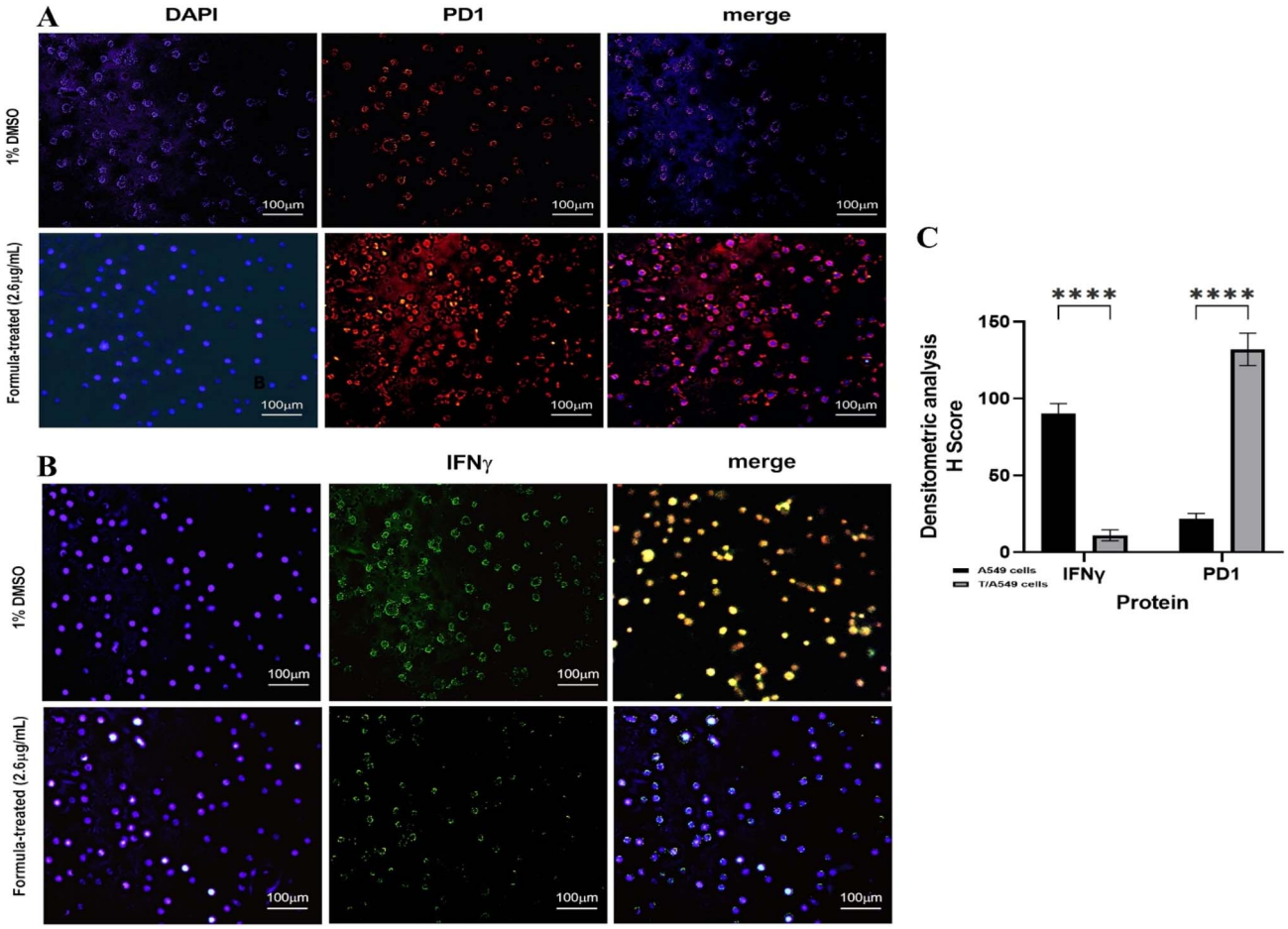


Fig. 9 Effects of BISDA on the expression of programmed cell death protein 1 (PD1) and interferon-gamma (IFN-γ) in A549 cells after treatment with the determined $IC_{50}$ (2.609 μg $mL^{-1}$) for 48 h using immunofluorescence staining (IF). (A) Representative photomicrographs of untreated and treated cells stained with PD-1 (red fluorescence) and DAPI (blue fluorescence). (B) Representative photomicrographs of untreated and treated cells stained with IFN-γ (green fluorescence) and DAPI (blue fluorescence). Overlay of DAPI with PD1 or IFN-γ in the merged photomicrographs reveals colocalization. Images were captured at 20× magnification. Scale bars, 100 μm. (C) H-score protein expression of PD-1 and IFN-γ in the untreated and treated groups. ****$p < 0.0001$ indicates differences between untreated and treated groups. Data are presented as mean ± SEM, $n = 3$ per condition.

HSP90, leading to a significant reduction in tumor initiation, progression, metastasis, and resistance to therapy.[68]

The correlational heatmap of A549 cells treated with BISDA (Fig. 10B) showed significant pathway reconfiguration, revealing the potential mechanisms. This represents a current limitation in our mechanistic understanding, warranting further dedicated investigation, particularly given the observed downregulation of TGF-β mRNA. TGFβ correlates positively with AKT1 ($r = 0.94$) and MAPK3 ($r = 0.73$), forming an axis with HSP90 (AKT1-HSP90 $r = 0.97$; MAPK3-HSP90 $r = 0.99$). TGFβ correlates positively with AKT1 ($r = 0.94$) and MAPK3 ($r = 0.73$), forming an axis with HSP90 (AKT1-HSP90 $r = 0.97$; MAPK3-HSP90 $r = 0.99$).[69,70] HSP70 correlated negatively with mTOR ($r = -0.88$), indicating a trade-off between proliferation and repair, whereas HSP60 was inversely related to MAPK3/AKT1. HSP70 correlated with mTOR ($r = -0.88$), showing a trade-off between proliferation and repair, whereas HSP60 was inversely related to MAPK3/AKT1. This analysis showed that BISDA targets EGFR, triggering TGFβ/AKT survival mechanisms. The negative correlations between cluster 1 (EGFR-mTOR) and cluster 2 (TGFβ-AKT1-MAPK3-HSP90) suggest pathway decoupling, matching the effects of selenadiazole on ROS-mediated damage.[71] HSP90 clustering with AKT1 and MAPK3 showed its chaperone role; BISDA may target HSP90, causing protein misfolding. HSP70's negative link between mTOR can enhance growth suppression.[72] These correlations may affect the PD1/IFN-γ pathways, as BISDA disruption of EGFR-MAPK could reduce immune evasion and amplify these effects.[73–75]

Principal component analysis (PCA) of signaling proteins (EGFR, TGF-β, mTOR, and AKT1) in A549 LUAD cells was assessed following 48 h of treatment with 2.609 μg $mL^{-1}$ of the BISDA compound compared to the untreated group. The first principal component (PC1) accounted for 90.7% of the total variance (Fig. 10C), which indicated treatment-linked variability. Untreated samples (red circles) were along the negative PC1 axis, whereas treated samples (cyan triangles) were clustered on the positive PC1 axis, indicating consistent signaling

 

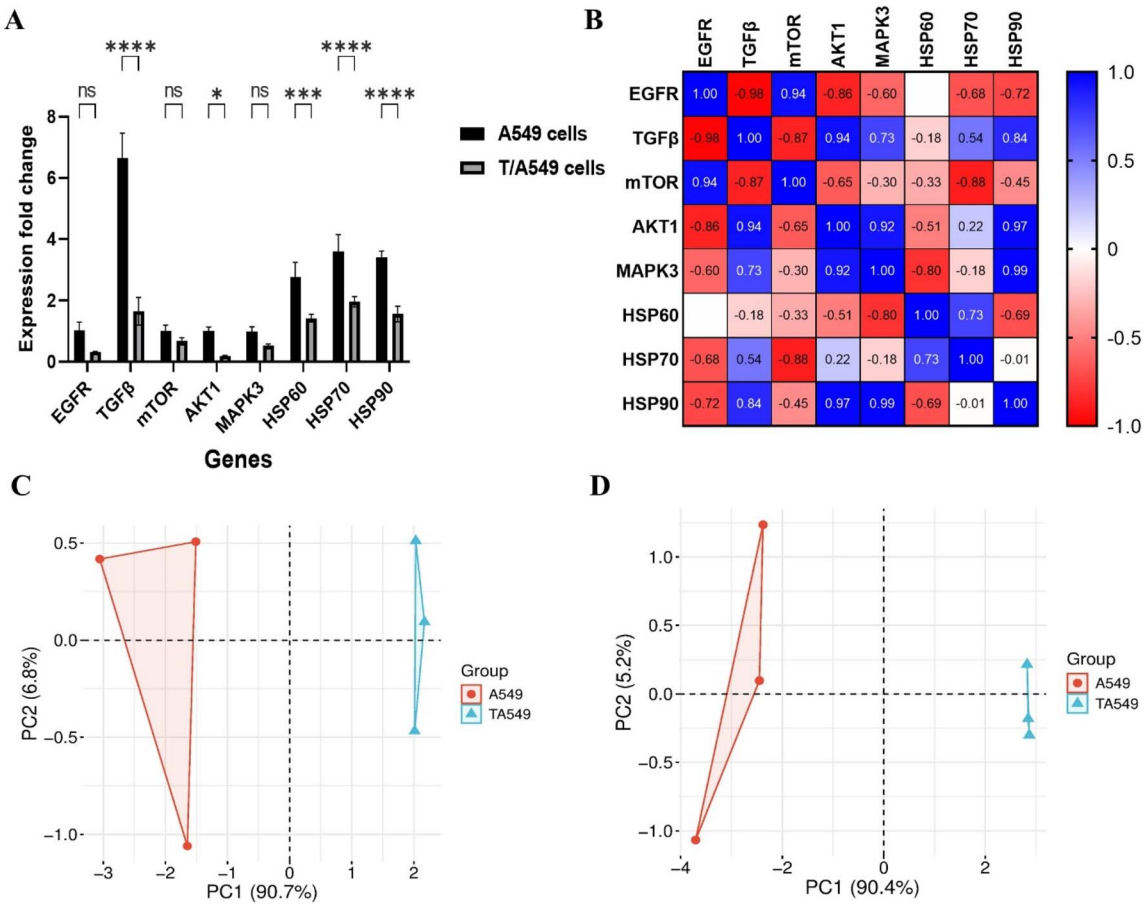


Fig. 10 Effects of BISDA on relative gene expression in A549 cells after treatment with $IC_{50}$ (2.609 μg $mL^{-1}$) for 48 h. (A) Relative mRNA expression (fold change) of *EGFR*, *TGF-β*, *mTOR*, *AKT1*, *MAPK3*, *HSP60*, *HSP70*, and *HSP90*. (B) Heat map of *EGFR*, *TGF-β*, *mTOR*, *AKT1*, *MAPK3*, *HSP60*, *HSP70*, and *HSP90* genes. Principal component analysis (PCA) for signalling proteins (EGFR, TGF-β, mTOR, and AKT1) (C) and HSP proteins (D) in untreated (red circles) and treated (cyan triangles) groups. *$p < 0.05$, ***$p < 0.001$, ****$p < 0.0001$ indicate differences between untreated and treated groups. Data are presented as mean ± SEM, $n = 3$ in each condition. EGFR: epidermal growth factor receptor. TGF-β: transforming growth factor-β. AKT1: protein kinase B. MAPK3: mitogen-activated protein kinase 3. mTOR: mechanistic target of rapamycin. HSP: heat shock protein.

profiles. PC1 accounted for 90.4% of the variance (Fig. 10D), while PC2 accounted for 5.2%. PC1 accounted for 90.4% of the variance (Fig. 10D), while PC2 accounted for 5.2%. The bioactive groups of BISDA exhibited anticancer potential through oxidative stress and apoptosis (Fig. 6C) and HSP inhibition (Fig. 10A). The bioactive groups of BISDA demonstrated anticancer potential through oxidative stress and apoptosis (Fig. 6C) and HSP inhibition (Fig. 10A). The transition to positive PC1 for treated cells indicates that BISDA modifies HSP patterns, involving HSP changes that cause cytotoxicity (Fig. 3D and 4C). The bioactive groups of BISDA showed anticancer potential through oxidative stress and apoptosis (Fig. 6C) and HSP inhibition (Fig. 10A). The transition to positive PC1 for treated cells indicates that BISDA modifies HSP patterns, involving HSP changes that cause cytotoxicity (Fig. 3D and 4C). BISDA may produce ROS, disrupt HSP-folding (Fig. 10A), or trigger HSP-mediated apoptosis (Fig. 6C). The PCA separation shows treatment alters HSP proteome from "protective" to "pro-apoptotic" state.

### 3.10. The physiochemical properties and absorption profile

To complement this *in vitro* cytotoxicity and mechanistic data, an ADMET (Absorption Distribution Metabolism Excretion and Toxicity) *in silico* prediction of BISDA properties was performed using the pkCSM platform to gain initial insight into its solubility and pharmacokinetic behaviour. As shown in Table 2, the model predicted a water solubility of −3.497 log mol per L, which is consistent with relatively low intrinsic aqueous solubility in addition to moderate-to-high human intestinal absorption (74.51%) and favorable Caco-2 permeability (0.776 log *P*app ($10^{-6}$ cm $s^{-1}$)) such that permeability represents a partial compensation for the limited solubility at the intestinal level. BISDA had a low predicted volume of distribution (VDss = −0.232 log *L* per kg) and fraction unbound (Fu = 0.099), consistent with high plasma protein binding and limited tissue penetration, combined with negative values for both blood–brain barrier permeability and central nervous system permeability (−1.741 log BB to −4.07 log PS, respectively), indicating little brain exposure as well as a high likelihood that there

Table 2 Physiochemical properties, absorption, and distribution profiles of BISDA

| Physiochemical properties | | | | | | |
|---|---|---|---|---|---|---|
| Descriptor | MW | Log *P* | Rotatable bonds | H-bond acceptors | H-bond donors | tPSA |
| Value | 594.37 | 0.37 | 6 | 10 | 2 | 199.13 Å$^2$ |

| Absorption profile | | | | | | |
|---|---|---|---|---|---|---|
| Parameter | Water solubility | Caco-2 permeability | Human intestinal absorption | Skin permeability | *P*-Glycoprotein substrate | *P*-Glycoprotein I/II inhibitor |
| Predicted value | −3.497 log mol per L | 0.776 log *P*app ($10^{-6}$ cm s$^{-1}$) | 74.51% | −2.735 log $K_p$ | Yes | Yes |

| Distribution profile | | | | |
|---|---|---|---|---|
| Parameter | Volume of distribution (VDss) | Fraction unbound (Fu) | BBB permeability | CNS permeability |
| Predicted value | −0.232 log *L* per kg | 0.099 | −1.741 log BB | −4.07 log PS |

would be no CNS-related adverse effects from agents affecting the central nervous system measured from the data collected here for BISDA.[76] Though experimental plasma solubility and kinetic solubility are not yet available, these rich computational descriptors afford a first guess at BISDA's physiological activity profile and identify solubility and distribution as point of emphasis for eventual optimization and formulation studies.

### 3.11. Possible mechanism of action of BISDA compound

EGFR activates downstream pathways, including PI3K/AKT/mTOR and RAS/RAF/MAPK/ERK pathways.[18] Several malignancies, including LUAD, exhibit EGFR overexpression, which activates pathways involved in cancer progression through proliferation, migration, angiogenesis, and decreased apoptosis.[6,77,78] Selenadiazole imino sulfonylbis (BISDA) contains bioactive compounds with anticancer activity that inhibit EGFR and its downstream pathways. Our results demonstrated that BISDA treatment of LUAD A549 cells downregulated EGFR gene expression and the downstream pathway genes mTOR, AKT1, and MAPK3 (Fig. 10A). The PI3K/AKT/mTOR pathway is crucial for cellular proliferation, growth, migration, and metabolism.[79,80] Downregulation of EGFR, AKT1, and mTOR expression after BISDA treatment (Fig. 10A–C) contributed to slower S-phase progression and G2/M phase arrest (Fig. 7A–C) and reduced cell migration (Fig. 8A–C) that induce cell proliferation. The MAPK/ERK pathway regulates cell proliferation, apoptosis, differentiation, and stress response.[81] The antiproliferative (Fig. 4A–C) and apoptotic (Fig. 6A–C) activities of BISDA could be due to the reduced expression of EGFR and MAPK3 (Fig. 10A). TGF-β activates the EGFR pathway through the Smad3 and ERK/Sp1 pathways to induce migration in breast cancer cells.[82,83] The reduced EGFR expression after BISDA treatment could be due to decreased TGF-β expression (Fig. 10A and C), which inhibited cell migration (Fig. 8A–C). Heat shock proteins regulate cancer migration, invasion, proliferation, and drug resistance as cancer biomarkers.[84,85] EGFR activation induces HSP70 phosphorylation,[86] whereas suppressing HSP90 inhibits EGFR signalling.[87] Decreased expression of HSP60, HSP70, and HSP90 was accompanied by reduced EGFR expression (Fig. 10A and D), indicating cell cycle arrest (Fig. 7A–C).

Moreover, IFN-γ can stimulate the activation of EGFR and its downstream MAPK/ERK pathway in brain cancer and intestinal epithelial cells.[88,89] As there was a positive correlation between IFN-γ, EGFR, and MAPK, the decrease in the protein expression of IFN-γ (Fig. 9B and C) after treatment could explain the downregulation of EGFR and MAPK gene expression (Fig. 10A). Moreover, PD-1 upregulation and PI3K/AKT/mTOR Inhibition has synergistic antitumor Action through the dual modulation that is considered typical therapeutic. Inhibiting PI3K/AKT/mTOR directly kills cancer cells or sensitizes them to apoptosis/autophagy, while PD-1/PD-L1 axis tweaks boost immune attack. Additionally, BISDA induced proliferation inhibition and cell cycle arrest, induce apoptosis, and enhance immunity (higher PD-1 but lower PD-L1, leading to net activation). This reduces tumor weight, migration, with no evidence of promoting proliferation.[90]

### 3.12. Position BISDA relative to existing selenium-based structurally related drugs

To contextualize the impact of BISDA within organoselenium therapeutics, comparison of its structure–activity relationship to known selenium-based drugs in development (*e.g.*, ebselen, ethaselen) is helpful. Ebselen, a single Se–N heterocycle containing a benzisoselenazol3(2*H*)-one core, imitates the activity of glutathione peroxidase and boasts an antioxidant and anti-inflammatory action, with its pharmacology primarily determined through redox modulation at a relatively small number of targets.[91] Ethaselen, a small-molecule organoselenium agent derived from the simple Se-containing scaffold recently has been developed as a redox-active anticancer compound targeting thiol-dependent enzymes (*e.g.*, TrxR) to upregulate oxidative

 

stress in tumor cells while retaining its selenium pharmacophore mononuclearity.[92] By contrast, BISDA is a sulfonyl-bridged bis(1,3,4-selenadiazole) system that adopts a $C_2$ symmetric architecture with π-extended framework in which two selenium-containing heterocycles are connected by a para-phenylene sulfone spacer and capped with acetylimino units. This design has higher selenium center density, hydrogen-bonding motifs, and conjugated aromatic surfaces than ebselen, ethaselen or ebselen-like molecules should allow such multivalency to engage protein and nucleic acids. Mechanistically, BISDA disturbs redox homeostasis and in concert activates positive effects on EGFR/PI3K/AKT/mTOR and HSP-associated signalling that cause apoptosis, G2/M arrest and decreased migration of LUAD cells while current selenium agents have mostly centred around ROS modulation or more limited pathways. These features set BISDA apart from simpler selenium pharmacophores by establishing it as a next-generation organoselenium scaffold where bisselenadiazole core, sulfonyl bridge and acetylimino termini work in concert to synergize selenium-fuelled oxidative stress with multinode inhibition of oncogenic signaling.

## 4 Conclusion

BISDA demonstrates anticancer efficacy against LUAD as a chemotherapeutic agent by inhibiting proliferation, migration, and cell cycle progression, while inducing apoptosis through downregulation of EGFR and the downstream PI3K/AKT/mTOR and MAPK/ERK pathways, mediated by TGF-β and IFN-γ. Selenadiazole derivatives containing imino and sulfone groups address LUAD by affecting pathways essential for cancer cell survival. Selenium compounds exhibit anticancer properties by modulating redox processes and inducing ROS accumulation in cancer cells, leading to damage of proteins, lipids, and DNA, ultimately resulting in cell death. Heat shock proteins (HSPs) are sensitive to oxidative stress, and selenium-induced ROS accumulation can overwhelm HSP60, HSP70, and HSP90, causing protein misfolding and activating apoptotic pathways. Selenium compounds modulate heat shock factors (HSFs), disrupting HSP upregulation during therapeutic stress. The incorporation of imino and sulfone groups into selenadiazole scaffolds enhances these effects through selective tumor accumulation. These molecules exploit differences between cancerous and normal cells, including elevated oxidative stress and heat shock protein-mediated protein homeostasis. This study demonstrates BISDA's anticancer efficacy in LUAD; however, it was limited to a single cell line model (A549), potentially overlooking NSCLC subtype heterogeneity and patient variability, thereby restricting generalizability. *In vitro* assays cannot fully replicate the complex tumor microenvironment, including immune cell interactions and systemic pharmacokinetics, which are critical for assessing BISDA's bioavailability and safety. Comparisons were restricted to cisplatin and did not evaluate BISDA against modern targeted therapies or immunotherapies, potentially hindering its optimal positioning in combinatorial regimens. These limitations underscore the need for expanded preclinical trials to validate therapeutic efficacy and safety.

## Author contributions

Conceptualization, WAE, HSH, ARS, NBH; methodology, AG, RFME, SAH, AAMR, HSH, software, HSH, RFME, WAE, AG; validation, RFME, HSH, SAH, AG; formal analysis, WAE, HSH, ARS, NBH, AMR; investigation, AG, RFME, SAH, AAMR, HSH; data curation, HSH, NBH, RFME, AG; writing – review & editing, WAE, HSH, ARS, NBH, AMR, SAH, RFME, AG; visualization, AG, RFME, SAH, AAMR, HSH; funding acquisition and project administration, WAE.

## Conflicts of interest

The authors declare that they have no known competing financial interests or personal relationships that could have influenced the work reported in this study.

## Data availability

The data that support the findings of this study are available within the main manuscript.

## Acknowledgements

This work was supported and funded by the Deanship of Scientific Research at Imam Mohammad Ibn Saud Islamic University (IMSIU) (grant number IMSIU-DDRSP2601).

## References

1 J. Zhou, Y. Xu, J. Liu, L. Feng, J. Yu and D. Chen, *Cancer Epidemiol.*, 2024, **93**, 102693.
2 S. F. Kadasah and A. M. S. Alqahtani, *Int. J. Mol. Sci.*, 2025, **26**, 6532.
3 Y. Gu, R. Yang, Y. Zhang, M. Guo, K. Takehiro, M. Zhan, L. Yang and H. Wang, *Mol. Biomed.*, 2025, **6**, 2.
4 C. Ding, R. Yao, Y. Wang, H. Liu, C. Li and H. Xie, *Front. Pharmacol*, 2025, **16**, 1656372.
5 A. Glaviano, A. S. C. Foo, H. Y. Lam, K. C. H. Yap, W. Jacot, R. H. Jones, H. Eng, M. G. Nair, P. Makvandi and B. Geoerger, *Mol. Cancer*, 2023, **22**, 138.
6 M. S. Ayoup, I. Shawki, H. Abdel-Hamid, D. A. Ghareeb, A. Masoud, M. F. Harras, M. El-Atawy, N. S. Alharbi and M. M. F. Ismail, *RSC Adv.*, 2024, **14**, 16713–16726.
7 S. Garbo, S. Di Giacomo, D. Łażewska, E. Honkisz-Orzechowska, A. Di Sotto, R. Fioravanti, C. Zwergel and C. Battistelli, *Pharmaceutics*, 2022, **15**, 104.
8 Y. Yuan, Y. Li, Q. Deng, J. Yang and J. Zhang, *ACS Omega*, 2024, **9**, 20919–20926.
9 R. Das, D. R. Chatterjee, S. Kapoor, H. Vyas and A. Shard, *RSC Med. Chem.*, 2024, **15**, 3070–3091.
10 M. Stępnik, M. Ferlińska, A. Smok-Pieniążek, D. Gradecka-Meesters, J. Arkusz and M. Stańczyk, *Toxicol. in Vitro*, 2011, **25**, 1075–1084.

11 N. S. Karuppiah, B. Sivapathasundharam, R. M. Chockalingam, P. K. Bhupathy, G. Kalaimani and R. S. Ramamurthi, *Cureus*, 2024, **16**, e51692.
12 L. Zhao, J. Chen, M.-F. Xu, Y.-H. Zhou, F. Ding, B.-H. Li, H.-M. Li, Y.-X. Zhang and C.-Z. Wu, *Bioorg. Chem.*, 2025, **166**, 109135.
13 R. Michalkova, L. Mirossay, M. Gazdova, M. Kello and J. Mojzis, *Cancers*, 2021, **13**, 2730.
14 I. B. Pavlinac, L. Persoons, A. Beč, L. Vrban, D. Daelemans, R. Vianello and M. Hranjec, *Bioorg. Chem.*, 2025, **154**, 107991.
15 K. Appalanaidu, R. Kotcherlakota, T. L. Dadmal, V. S. Bollu, R. M. Kumbhare and C. R. Patra, *Bioorg. Med. Chem. Lett.*, 2016, **26**, 5361–5368.
16 T. M. Wrodnigg, A. J. Steiner and B. J. Ueberbacher, *Anti-Cancer Agents Med. Chem.*, 2008, **8**, 77–85.
17 Y. Jiang, M. Chen, H. Nie and Y. Yuan, *Hum. Vaccines Immunother.*, 2019, **15**, 1111–1122.
18 P. C. Hsu, D. M. Jablons, C. T. Yang and L. You, *Int. J. Mol. Sci.*, 2019, **20**, 3821.
19 J. Whooley, M. Alazzawi, N. E. Donlon, J. C. Bolger and W. B. Robb, *Dis. Esophagus*, 2022, **35**, doab063.
20 M. R. Zaidi and G. Merlino, *Clin. Cancer Res.*, 2011, **17**, 6118–6124.
21 X. Liu, *Pathol., Res. Pract.*, 2025, **272**, 156046.
22 M. Rosado-Sanz, N. Martínez-Alarcón, A. Abellán-Soriano, R. Golfe, E. M. Trinidad and J. Font de Mora, *Biomedicines*, 2025, **13**, 1945.
23 R. F. M. Elshaarawy, J. Dechnik, H. M. A. Hassan, D. Dietrich, M. A. Betiha, S. Schmidt and C. Janiak, *J. Mol. Liq.*, 2018, **266**, 484–494.
24 R. F. M. Elshaarawy, T. B. Mostafa, A. A. Refaee and E. A. El-Sawi, *RSC Adv.*, 2015, **5**, 68260–68269.
25 S. E. I. Elbehairi, M. Y. Alfaifi, A. A. Shati, M. A. Alshehri, R. F. M. Elshaarawy and H. S. Hafez, *Chem. Biol. Drug Des.*, 2020, **96**, 1148–1161.
26 R. F. M. Elshaarawy, H. R. Z. Tadros, R. M. Abd El-Aal, F. H. A. Mustafa, Y. A. Soliman and M. A. Hamed, *J. Environ. Chem. Eng.*, 2016, **4**, 2754–2764.
27 A. R. E. Mahdy, O. A. A. Ali, W. M. Serag, E. Fayad, R. F. M. Elshaarawy and E. M. Gad, *J. Mol. Struct.*, 2022, **1259**, 132726.
28 S. Gomha, T. Farghaly, A. R. Sayed and M. M. Abdalla, *J. Heterocycl. Chem.*, 2015, **53**, 1505–1511.
29 M. Hazekawa, T. Nishinakagawa, T. Kawakubo-Yasukochi and M. Nakashima, *Exp. Ther. Med.*, 2019, **18**, 3197–3205.
30 R. C. Wilkins, B. C. Kutzner, M. Truong, J. Sanchez-Dardon and J. R. McLean, *Cytometry*, 2002, **48**, 14–19.
31 D. B. Asante, M. Morici, G. Mohan, E. Acheampong, I. Spencer, W. Lin, P. van Miert, S. Gibson, A. B. Beasley, M. Ziman, L. Calapre, T. M. Meniawy and E. S. Gray, *Cancers*, 2021, **13**, 6225.
32 R. E. Kingston, P. Chomczynski and N. Sacchi, *Curr. Protoc. Mol. Biol.*, 1996, **36**, 1–9.
33 J. Kuang, X. Yan, A. J. Genders, C. Granata and D. J. Bishop, *PLoS One*, 2018, **13**, e0196438.
34 A. Abdelhamid, M. Sallam and S. Amer, *Heteroat. Chem.*, 2001, **12**, 468–474.
35 F. Zaera, *Chem. Soc. Rev.*, 2014, **43**, 7624–7663.
36 Z. Moussa, A. Perez Paz, M. A. Khalaf, Z. M. A. Judeh, A. Alzamly, A. Samadi, J. H. Al-Fahemi, M. B. Tatina, H. T. Al-Masri, R. S. Jassas and S. A. Ahmed, *Chem.–Asian J.*, 2023, **18**, e202300475.
37 P. Majumdar, A. Pati, M. Patra, R. K. Behera and A. K. Behera, *Chem. Rev.*, 2014, **114**, 2942–2977.
38 R. Huang, B. Gu, M. Wang, Y. Zhao and X. Jiang, *Molecules*, 2024, **29**, 4137.
39 J. Ruiz, L. García, C. Mejuto, M. Vivanco, M. R. Díaz and S. García-Granda, *Chem. Commun.*, 2014, **50**, 2129–2132.
40 G. F. Pauli, S.-N. Chen, D. C. Lankin, J. Bisson, R. J. Case, L. R. Chadwick, T. Gödecke, T. Inui, A. Krunic, B. U. Jaki, J. B. McAlpine, S. Mo, J. G. Napolitano, J. Orjala, J. Lehtivarjo, S.-P. Korhonen and M. Niemitz, *J. Nat. Prod.*, 2014, **77**, 1473–1487.
41 F. L. Gabriel, M. Cyris, W. Giger and H. P. Kohler, *Chem. Biodiversity*, 2007, **4**, 2123–2137.
42 R. Das, D. R. Chatterjee, S. Kapoor, H. Vyas and A. Shard, *RSC Med. Chem.*, 2024, **15**, 3070–3091.
43 T. Chen, W. Zheng, Y. S. Wong and F. Yang, *Biomed. Pharmacother.*, 2008, **62**, 77–84.
44 D. Plano, E. Moreno, M. Font, I. Encío, J. A. Palop and C. Sanmartín, *Arch. Pharm.*, 2010, **343**, 680–691.
45 A. C. Ruberte, D. Plano, I. Encío, C. Aydillo, A. K. Sharma and C. Sanmartín, *Eur. J. Med. Chem.*, 2018, **157**, 14–27.
46 D. Radomska, R. Czarnomysy, D. Radomski and K. Bielawski, *Int. J. Mol. Sci.*, 2021, **22**, 1009.
47 C. Gallo-Rodriguez and J. B. Rodriguez, *ChemMedChem*, 2024, **19**, e202400063.
48 S. Anjum, M. Hashim, M. Imran, S. Babur, S. Adnan, C. Hano and W. N. Ibrahim, *Cancer Rep.*, 2025, **8**, e70210.
49 A. Bansal and M. C. Simon, *J. Cell Biol.*, 2018, **217**, 2291–2298.
50 A. P. Fernandes and V. Gandin, *Biochim. Biophys. Acta*, 2015, **1850**, 1642–1660.
51 H. Zeng, M. Briske-Anderson, M. Wu and M. P. Moyer, *Nutr. Cancer*, 2012, **64**, 128–135.
52 G. He, J. Kuang, A. R. Khokhar and Z. H. Siddik, *Gynecol. Oncol.*, 2011, **122**, 402–409.
53 G. Li, H. U. Park, D. Liang and R. Y. Zhao, *Retrovirology*, 2010, **7**, 59.
54 R. Ramirez-Tagle, C. A. Escobar, V. Romero, I. Montorfano, R. Armisén, V. Borgna, E. Jeldes, L. Pizarro, F. Simon and C. Echeverria, *Int. J. Mol. Sci.*, 2016, **17**, 260.
55 T. Ji, C. Lin, L. S. Krill, R. Eskander, Y. Guo, X. Zi and B. H. Hoang, *Mol. Cancer*, 2013, **12**, 55.
56 J.-s. Wu, J. Jiang, B.-j. Chen, K. Wang, Y.-l. Tang and X.-h. Liang, *Transl. Oncol.*, 2021, **14**, 100899.
57 D. F. Veber, S. R. Johnson, H. Y. Cheng, B. R. Smith, K. W. Ward and K. D. Kopple, *J. Med. Chem.*, 2002, **45**, 2615–2623.
58 B. Kaur, G. Singh, V. Sharma and I. Singh, *Anti-Cancer Agents Med. Chem.*, 2023, **23**, 869–881.

59 N. M. Mhaidat, M. Al-Smadi, F. Al-Momani, K. H. Alzoubi, I. Mansi and Q. Al-Balas, *Drug Des., Dev. Ther.*, 2015, **9**, 3645–3652.
60 Q. Xie, Y. Zhou, G. Lan, L. Yang, W. Zheng, Y. Liang and T. Chen, *Biochem. Biophys. Res. Commun.*, 2014, **449**, 88–93.
61 M. Islam, S. Jones and I. Ellis, *Biomedicines*, 2023, **11**, 3001.
62 J. Massagué and D. Sheppard, *Cell*, 2023, **186**, 4007–4037.
63 A. W. t. MacFarlane, M. Jillab, E. R. Plimack, G. R. Hudes, R. G. Uzzo, S. Litwin, E. Dulaimi, T. Al-Saleem and K. S. Campbell, *Cancer Immunol. Res.*, 2014, **2**, 320–331.
64 S. Singh, S. Kumar, R. K. Srivastava, A. Nandi, G. Thacker, H. Murali, S. Kim, M. Baldeon, J. Tobias, M. A. Blanco, R. Saffie, M. R. Zaidi, S. Sinha, L. Busino, S. Y. Fuchs and R. Chakrabarti, *Nat. Cell Biol.*, 2020, **22**, 591–602.
65 D. Jorgovanovic, M. Song, L. Wang and Y. Zhang, *Biomark. Res.*, 2020, **8**, 49.
66 C. Weekley and H. Harris, *Chem. Soc. Rev.*, 2013, **42**, 8870–8894.
67 S. Debnath, A. Agarwal, N. Kumar and A. Bedi, *Future Pharmacol.*, 2022, **2**, 595–607.
68 S. Mittal and M. S. Rajala, *Cancer Biol. Ther.*, 2020, **21**, 477–485.
69 H. Zhang, Y. Cao, J. Tang and R. Wang, *BioMed Res. Int.*, 2022, **2022**, 9944847.
70 B. Lawal, Y. C. Kuo, A. T. Wu and H. S. Huang, *Am. J. Cancer Res.*, 2023, **13**, 2598–2616.
71 G. T. Kim, K. W. Hahn, S. Y. Yoon, K. Y. Sohn and J. W. Kim, *Cancers*, 2020, **12**, 560.
72 J. Moore, M. Megaly, A. J. MacNeil, P. Klentrou and E. Tsiani, *Biomed. Pharmacother.*, 2016, **83**, 725–732.
73 F. Zhou, H. Guo, Y. Xia, X. Le, D. S. W. Tan, S. S. Ramalingam and C. Zhou, *Nat. Rev. Clin. Oncol.*, 2025, **22**, 95–116.
74 A. Shiiya, T. Noguchi, U. Tomaru, S. Ariga, Y. Takashima, Y. Ohhara, J. Taguchi, S. Takeuchi, Y. Shimizu, I. Kinoshita, T. Koizumi, Y. Matsuno, N. Shinagawa, J. Sakakibara-Konishi and H. Dosaka-Akita, *Cancer Sci.*, 2022, 114.
75 T. G. Mhone, M. C. Chen, C. H. Kuo, T. C. Shih, C. M. Yeh, T. F. Wang, R. J. Chen, Y. C. Chang, W. W. Kuo and C. Y. Huang, *Int. J. Biol. Sci.*, 2022, **18**, 3636–3652.
76 C. Kramer, A. Ting, H. Zheng, J. Hert, T. Schindler, M. Stahl, G. Robb, J. J. Crawford, J. Blaney and S. Montague, *J. Med. Chem.*, 2017, **61**, 3277–3292.
77 L. K. Shawver, D. Slamon and A. Ullrich, *Cancer Cell*, 2002, **1**, 117–123.
78 K. Oda, Y. Matsuoka, A. Funahashi and H. Kitano, *Mol. Syst. Biol.*, 2005, **1**, 20050010.
79 A. Glaviano, A. S. C. Foo, H. Y. Lam, K. C. H. Yap, W. Jacot, R. H. Jones, H. Eng, M. G. Nair, P. Makvandi, B. Geoerger, M. H. Kulke, R. D. Baird, J. S. Prabhu, D. Carbone, C. Pecoraro, D. B. L. Teh, G. Sethi, V. Cavalieri, K. H. Lin, N. R. Javidi-Sharifi, E. Toska, M. S. Davids, J. R. Brown, P. Diana, J. Stebbing, D. A. Fruman and A. P. Kumar, *Mol. Cancer*, 2023, **22**, 138.
80 P. Friedl and K. Wolf, *Nat. Rev. Cancer*, 2003, **3**, 362–374.
81 Y. J. Guo, W. W. Pan, S. B. Liu, Z. F. Shen, Y. Xu and L. L. Hu, *Exp. Ther. Med.*, 2020, **19**, 1997–2007.
82 Y. Zhao, J. Ma, Y. Fan, Z. Wang, R. Tian, W. Ji, F. Zhang and R. Niu, *Mol. Oncol.*, 2018, **12**, 305–321.
83 M. K. Wendt, J. A. Smith and W. P. Schiemann, *Oncogene*, 2010, **29**, 6485–6498.
84 C. W. Yun, H. J. Kim, J. H. Lim and S. H. Lee, *Cells*, 2019, **9**, 60.
85 A. M. Cyran and A. Zhitkovich, *Front. Oncol.*, 2022, 12–2022.
86 Y. Wang, A. Fernandez, X. Pei, B. Liu, L. Shen, Y. Yan, H. S. Solanki, L. Yang, M. Zhou, Y. Guo, J. Wu, K. L. Reckamp, L. Zheng and B. Shen, *Nucleic Acids Res.*, 2024, **52**, 13057–13072.
87 S. A. Lang, D. Klein, C. Moser, A. Gaumann, G. Glockzin, M. H. Dahlke, W. Dietmaier, U. Bolder, H. J. Schlitt, E. K. Geissler and O. Stoeltzing, *Mol. Cancer Ther.*, 2007, **6**, 1123–1132.
88 X. Zhou, T. Liang, Y. Ge, Y. Wang and W. Ma, *Brain Sci.*, 2023, **13**, 1349.
89 G. Paul, R. R. Marchelletta, D. F. McCole and K. E. Barrett, *J. Biol. Chem.*, 2012, **287**, 2144–2155.
90 Y. Zakharia, A. Bhattacharya and Y. M. Rustum, *Oncotarget*, 2018, **9**, 10765–10783.
91 G. K. Azad and R. S. Tomar, *Mol. Biol. Rep.*, 2014, **41**, 4865–4879.
92 L. Wang, Z. Yang, J. Fu, H. Yin, K. Xiong, Q. Tan, H. Jin, J. Li, T. Wang and W. Tang, *Free Radicals Biol. Med.*, 2012, **52**, 898–908.